Peroxisome dysfunction alters metabolism of photoreceptor outer segments in human retinal pigment epithelium

Constantin Mouzaaber, [1] Carly B. Feldman, [2] Suzette M. Huguenin, [3] John Y.S. Han, [4] Erin Trombly, [4] Qitao Zhang, [4] Aja Rieger, [5] Hamed Hojjat, [1] Brandon C. Huynh, [1] Ehsan Misaghi, [1] Alina Radziwon, [1] Temesgen D. Fufa, [2] Robert B. Hufnagel,[2,6] Jason M.L. Miller, [4,7] Matthew D. Benson[1,*]

Affiliations:

[1]Department of Ophthalmology and Visual Sciences, University of Alberta, Edmonton, AB, Canada.

[2]Ophthalmic Genetics and Visual Function Branch, National Eye Institute, National Institutes of Health, Bethesda, MD, USA

[3]Peroxisomal Diseases Laboratory, Kennedy Krieger Institute, Baltimore, MD, USA

[4]Kellogg Eye Center, Department of Ophthalmology and Visual Sciences, University of Michigan, Ann Arbor, MI, USA

[5]Flow Cytometry Core Facility, Faculty of Medicine and Dentistry, University of Alberta, Edmonton, AB, Canada

[6]Center for Integrated Health Care Research, Kaiser Permanente, Hawai'i, Hawai'i Permanente Medical Group, Honolulu, HI, USA

[7]Cellular and Molecular Biology Program, University of Michigan, Ann Arbor, MI, USA

[*]Correspondence: mbenson@ualberta.ca

Key Words:

Peroxisome, peroxisome biogenesis disorder, PEX1, PEX6, retinal pigment epithelium

Abstract

Purpose. Peroxisomes are ubiquitous organelles that compartmentalize metabolic reactions including lipid catabolism and cellular detoxification. Biallelic loss-of-function variants in genes responsible for peroxisome assembly and function cause peroxisome biogenesis disorders (PBDs). Approximately three-quarters of PBDs are due to pathogenic variants in *PEX1* or *PEX6* and result in multisystem disease, including retinal degeneration and blindness. Despite retinal pigment epithelial (RPE) dysfunction and retinal degeneration occurring frequently in PBDs, precisely how impaired peroxisome activity disrupts retinal function remains to be fully explored. To address this, we differentiated *PEX1* knockout (*PEX1*$^{-/-}$), *PEX6* knockout (*PEX6*$^{-/-}$), and wildtype human induced pluripotent stem cells (iPSCs) into RPE to study the consequences of peroxisome dysfunction in this disease-relevant cell type.

Methods. CRISPR/Cas9-mediated genome editing was used to generate *PEX1*$^{-/-}$and *PEX6*$^{-/-}$in human iPSCs. The knockouts and isogenic wildtype iPSCs were differentiated into RPE (iRPE) and characterized by morphology, pigmentation, transepithelial electrical resistance (TEER), and expression of proteins associated with differentiated RPE using immunofluorescence microscopy

and flow cytometry. Immunoblot analysis of whole iRPE lysates was used to evaluate the proteolytic processing of peroxisome enzymes, a measure of the integrity of peroxisome matrix protein import. Immunofluorescence detection of peroxisome membrane proteins was used to determine the abundance of peroxisomes across iRPE lines. Targeted lipidomics by gas and liquid chromatography with mass spectrometry were used to quantitatively compare the profiles of wildtype, *PEX1*$_{-/-}$, and *PEX6*$_{-/-}$iRPE. Accumulation of intracellular neutral lipid, and more specifically lipid droplets, in iRPE was measured using flow cytometry and perilipin-2 immunoblotting, respectively. Phagocytosis of photoreceptor outer segments (POS) by iRPE was evaluated using rhodopsin immunoblotting.

Results. *PEX1*$_{-/-}$, *PEX6*$_{-/-}$, and wildtype iRPE all had comparable hexagonal morphology and integrity of tight junctions, developed pigment, and similarly expressed proteins characteristic of RPE. Immunoblot analysis demonstrated aberrant processing of ACOX1, MFP2, and ACAA1 in *PEX1*$_{-/-}$ and *PEX6*$_{-/-}$iRPE, suggesting impaired peroxisome matrix protein import. Targeted lipid profiling, including total fatty acid (FA) lipid profile analysis, revealed that in comparison to wildtype, *PEX1*$_{-/-}$ and *PEX6*$_{-/-}$iRPE had significantly reduced docosahexaenoic acid (C22:6ω3) ($p<0.001$) and phosphoethanolamine plasmalogens ($p<0.0001$ for C18:0(plasm)-Total-PE), while very long-chain fatty acids (VLCFA) ($p<0.001$ for C26:0 and $p<0.01$ for C26:1ω9) and branched-chain FAs ($p<0.01$ for both pristanic acid and phytanic acid) were significantly elevated. Following a POS challenge, wildtype iRPE had significantly elevated eicosapentaenoic acid (C20:5ω3) (p=9.3E-5) and arachidonic acid (C20:4ω6) (p=0.013), both retroconversion products from the two most abundant polyunsaturated FAs in POS: C22:6ω3 and docosapentaenoic acid (C22:5ω6). *PEX1*$_{-/-}$and *PEX6*$_{-/-}$iRPE accumulated twice the amount of C22:5ω6 ($p<0.05$) relative to wildtype iRPE following a POS challenge, without a significant

increase in C20:5ω3 or C20:4ω6, suggesting impaired ω3 and ω6 retroconversion pathways. Finally, *PEX1*$_{-/-}$and *PEX6*$_{-/-}$iRPE demonstrated delayed degradation of internalized POS based on rhodopsin immunoblotting, increased intracellular lipid droplets, and reduced TEER following a POS challenge.

Conclusions. Our work has established the first human iRPE models to study the effects of peroxisome dysfunction in the RPE. Impaired peroxisome activity resulted in significant lipid profile changes and defective phagocytosis in iRPE. Dysregulated POS metabolism in the RPE is a potential mechanism driving retinal degeneration in patients with PBDs. Fully understanding the role of peroxisomes in the RPE will facilitate the development of novel therapies for degenerative retinal disorders.

List of Abbreviations

AAA	ATPases Associated with Diverse Cellular Activities
ACAA1	Acetyl-Coenzyme A Acyltransferase 1
ACOX1	Acyl-Coenzyme A Oxidase 1
BCFAs	Branched-Chain Fatty Acids
DMEM	Dulbecco’s Modified Eagle Medium
DPBS	Dulbecco's Phosphate Buffered Saline
FAs	Fatty Acids
iPSCs	Induced Pluripotent Stem Cells

iRPE	iPSC-Derived RPE
IRDs	Inherited Retinal Dystrophies
LDs	Lipid Droplets
MFP2	Multifunctional Protein 2
PBDs	Peroxisome Biogenesis Disorders
POS	Photoreceptor Outer Segments
PTS1	Peroxisomal Targeting Signal-1
PTS2	Peroxisomal Targeting Signal-2
PUFA	Polyunsaturated Fatty Acids
RPE	Retinal Pigment Epithelium
RPE-MM	Retinal Pigment Epithelium Maturation Media
VLCFAs	Very Long-Chain Fatty Acids

Introduction

As a highly bioenergetic tissue, the retina is especially susceptible to local and systemic metabolic disturbances. Indeed, retinal degeneration occurs in a myriad of metabolic diseases, including peroxisomal biogenesis disorders (PBDs). [1] The PBDs are a group of recessively inherited diseases that result in impaired function of the brain, retina, liver, and kidneys, among

other organs, due to the disrupted synthesis and activity of peroxisomes. Peroxisomes are ubiquitous subcellular organelles that have essential roles in lipid metabolism and redox homeostasis via unique enzymes including ACOX1, MFP2 and ACAA1 that are guided into the peroxisome lumen using peroxisome targeting sequences 1 (PTS1) and 2 (PTS2). Two of the major reactions occurring in the peroxisome lumen are the β- and α-oxidation of lipid species such as very long-chain (≥ C22) and branched-chain fatty acids, to produce shortened or straightened FAs (≤C20) that may then undergo mitochondrial β-oxidation.

In the retina, peroxisomes metabolize very long (≥ C22)-chain polyunsaturated fatty acids (PUFAs), which are highly enriched in photoreceptor outer segments. [2] These outer segments are continuously phagocytosed and metabolized by the retinal pigment epithelium (RPE), suggesting a critical role for intact peroxisome function in the RPE. Mice with global deficiencies in peroxisomal activity have defective phagocytosis and perturbed fatty acid β-oxidation in the RPE, which is associated with the development of retinal degeneration. [3–6] However, the effect of peroxisome dysfunction in human RPE is understudied. To this end, we have developed cell-autonomous models to explore the function of peroxisomes in human RPE.

Pathogenic loss-of-function variants in 14 different *PEX* genes, encoding for peroxins essential for peroxisome assembly and activity, result in PBDs in humans, with *PEX1* and *PEX6* together accounting for 75% of cases. [1,7] PEX1 and PEX6 are members of the AAA ATPase (ATPases associated with diverse cellular activities) family and form a heterohexameric complex on the peroxisome membrane. This complex facilitates the recycling of the cargo-carrying shuttle,

PEX5, from the peroxisome membrane to the cytosol to enable subsequent rounds of peroxisomal matrix protein import. [1] Despite retinal degeneration and blindness occurring in the majority of patients with *PEX1*- and *PEX6*-related PBDs, [8] precisely how peroxisomal dysfunction impairs retinal function, and specifically induces RPE atrophy in humans, is largely unknown. To address this, we have generated and characterized the first human induced pluripotent stem cell-derived retinal pigment epithelium (iRPE) models, allowing us to study peroxisome dysfunction in a disease-relevant cell type. Our results demonstrate that *PEX1*deficient and *PEX6*-deficient iPSCs can be differentiated into mature RPE but have cell-autonomous defects in lipid metabolism and impaired phagocytosis of photoreceptor outer segments, highlighting a novel disease mechanism in the RPE in PBDs. In addition, our iRPE models serve as novel *in vitro* platforms to broaden our understanding of the integral roles of peroxisomes in the RPE.

Methods

Cell Culture

All cells were incubated at 37 °C and 5% CO2 in a Heracell VIOS 160i incubator (Thermo Scientific, Cat. No. 51033546). Matrix-coated culture dishes were prepared using Matrigel (Corning, Cat. No. 354234) that was diluted in DMEM/F12 (Thermo Scientific, Cat. No. 11330032) to yield 10µg/cm2 or 100µg/mL according to manufacturer protocols.

A normal human iPSC line (Gibco™ episomal hiPSC, Thermo Scientific, Cat. No. A18945) was used to derive single isogenic *PEX1*$_{-/-}$and *PEX6*$_{-/-}$iPSC clones (generated by Synthego, USA using CRISPR/Cas9-mediated genome editing). All lines were cultured in TeSR™-E8™ media (StemCell Technologies, Cat. No. 05990, Canada), and passaged using ReLeSR™ (StemCell Technologies, Cat. No. 100-0484, Canada). Ethics approval was obtained for the use of human iPSCs for research (Pro00074451).

iRPE were maintained in RPE Maturation Media (RPE-MM) composed of Minimal Essential Medium α (Thermo Scientific, Cat. No. 41061029) supplemented with 2% fetal bovine serum (Millipore Sigma, Cat. No. F1051), 2% KnockOut serum replacement (Thermo Scientific, Cat. No. 10828028), 1x non-essential amino acids (Cytiva, Cat. No. SH3023801 -100x), 1x penicillin/streptomycin (Cytiva, Cat. No. SV30010 -100x), 0.5x N-2 supplement (Thermo Scientific, Cat. No. 175020DPBS48 -100x), 250 µg/mL taurine (Sigma Aldrich, Cat. No. T869125G), 14 pg/mL triiodo-L-thyronine (Sigma Aldrich, Cat. No. T5516), and 20 ng/mL hydrocortisone (Sigma Aldrich, Cat. No. H0888) dissolved in Dulbecco's Phosphate Buffered Saline (DPBS) (Cytvia, Cat. No. 12 SH30028.02). The formulation was derived from a published protocol. [9] iRPE were passaged using TrypLE™ (Thermo Scientific, Cat. No. 12563011).

iPSC-RPE Differentiation

iPSC-RPE differentiation media recipe was derived from a published protocol[10] and consisted of HyClone Dulbecco's Modified Eagle Medium (DMEM) with high glucose (Cytiva, Cat. No. SH30243.01) supplemented with 1x non-essential amino acids (Cytiva, Cat. No. SH3023801 -100x) and 20% KnockOut serum (Thermo Scientific, Cat. No. 10828028). The media was

filtered through a 0.2 µm pore size vacuum filter (Thermo Scientific, Cat. No. 568-0020). The media was changed 3 times per week. At each media change, 50 µM of 2-mercaptoethanol (BioRad, Cat. No. 1610170) was added.

iPSC cultures were harvested using TrypLE™ (Thermo Scientific, Cat. No. 12563011), and single-cell suspension of iPSCs were seeded at 40,000 cells/cm^2 with TeSR™-E8™ medium supplemented with 2.5 µM blebbistatin (SigmaAldrich, Cat. No. B0560). The following day, TeSR™-E8™ medium without blebbistatin was used until the cells reached 70% confluency. Differentiation then commenced (Figure 1, Day 0) by incubating the cells with differentiation media as outlined below:

For the first week, 10 mM nicotinamide (StemCell Technologies, Cat. No. 07154) was added to the differentiation medium between Day 0 and Day 7. For the second week, 100 ng/mL Activin-A (StemCell Technologies, Cat. No. 78001) was added to the differentiation medium between Day 7 and Day 14. For the following 4 weeks, 3 µM CHIR99021 (StemCell Technologies, Cat. No. 72054) was added to the differentiation medium between Day 14 and Day 42, after which the cells reached a committed RPE stage. At Day 43, cells were harvested using TrypLE™ (Thermo Scientific, Cat. No. 12563011), and either pooled for cryopreservation or RPE maturation proceeded by generating a single-cell suspension, seeding 300,000 cells/cm^2 , and maintaining the cells in RPE-MM for 3 additional weeks. At Day 63, iRPE cells were similarly harvested and seeded at 300,000 cells/cm^2 while supplementing the media with 10 µM Y-27632 (StemCell Technologies, Cat. No. 72304, Canada) during seeding. The cells were considered mature RPE three weeks after their final seeding. iRPE from independent wells were used for experimental replicates.

Validating Knockout of PEX1 and PEX6 in iRPE

Sanger sequencing performed for *PEX1*-/-iRPE confirmed a homozygous variant c.178dup; p.(W60Lfs*8) in *PEX1* (NM_000466.3) in exon 2 of 24 (Supplementary Figure 1A). Sanger sequencing performed for *PEX6*-/-iRPE confirmed a homozygous variant c.197dup; p.(Q67Afs*11) in *PEX6* (NM_000287.4) in exon 1 of 17 (Supplementary Figure 1B).

iPSC Transfection

iPSC colonies were cultured on Matrigel-coated chamber slides (Sarstedt, Cat. No. 946170802). Each well was transfected with 300 ng of GFP-SKL (Addgene, plasmid #53450) or pmaxGFP® (Lonza) using Lipofectamine 2000 (Invitrogen, Cat. No. 11668019) for 48 hours. The cells were fixed with 4% paraformaldehyde (Sigma Aldrich, Cat. No. P6148-500G), incubated with 1.67 μ M DAPI (Millipore Sigma, Cat. No. D8417) for 5 minutes at room temperature, and mounted with ProLong™ Glass Antifade Mountant (Thermofisher, Cat. No. P36984) following DPBS washes between steps.

Western Blotting

Cells were harvested mechanically with cell scrapers in radioimmunoprecipitation (RIPA) buffer (Thermo Scientific, Cat. No. 89900) supplemented with cOmplete™ Protease Inhibitor Cocktail (Sigma Aldrich, Cat. No. 11697498001).

Protein concentration was determined using Pierce™ BCA Protein Assay Kit (Thermo Scientific, Cat. No. 23225). Multiskan™ GO Microplate Spectrophotometer (Thermo Scientific, Cat. No. 51119300) was used to measure absorbance at 562 nm.

Samples were mixed with 1x Laemmli Sample Buffer (Bio-Rad, Cat. No. 1610747 – 4x) supplemented with 10% 2-mercaptoethanol (Sigma Aldrich, Cat. No. M3148) and incubated at 70 °C for 10 minutes. Samples were then loaded onto 4-15% Mini-PROTEAN® TGX™ Precast Protein Gels precast (Bio-Rad, Cat. No. 4561084) housed in Mini-PROTEAN® Tetra Cell (Bio-Rad, Cat. No. 1658037) submerged with 1 L of running buffer (25 mM Tris, 190 mM glycine, 0.1% SDS). Following electrophoresis at 100 V for 120 minutes, proteins were transferred to a nitrocellulose membrane (Thermo Scientific, Cat. No. IB23002) at 23 V for 6 minutes with the iBlot™ 2 dry blotting system (Thermo Scientific, Cat. No. IB21001).

Membranes were protected from light and incubated with Intercept® PBS Blocking Buffer (Li-Cor, Cat. No. 927-70001) for 1 hour at room temperature. All incubations and washes were performed on a rocker. A 1:1 blocking buffer:PBS-T (PBS containing Tween-20 0.05%) solution was prepared to dilute antibodies for incubations. Primary antibodies (Supplementary Table 1) were applied overnight at 4 °C. After the incubation, membranes were washed with PBS-T three times for 5 minutes each. Secondary antibodies (Supplementary Table 1) were applied for 1 hour at room temperature. Following the incubation, membranes were washed with PBS-T twice for 10 minutes each and then once with PBS for 10 minutes.

Membranes were scanned using the Odyssey CLx imaging system (Li-Cor) and visualized on Image Studio (LiCor, V.5.2). Blots were captured with a high-quality setting at 169 µm resolution. Regions of interest were manually selected and densitometry values were recorded.

Values were adjusted using their respective loading controls and normalized to wildtype using Microsoft® Excel® (Version 2401 Build 16.0.17231.20236)

Immunofluorescence Microscopy

Cells were grown on Matrigel-coated chamber slides (Ibidi, Cat. No.81817) and were washed once with DPBS and then incubated on ice with 4% paraformaldehyde (Sigma Aldrich, Cat. No. P6148-500G) for 15 minutes. Cells were then washed 3 times with DPBS and blocked and permeabilized by incubation in PBS supplemented with 0.1% saponin (Millipore Sigma, Cat. No. 558255) and 1% bovine serum albumin (Sigma Aldrich, Cat. No. A9418) for 30 minutes at room temperature. Incubation with primary antibodies occurred for 1 hour at room temperature in blocking buffer. Cells were then washed 3 times with DPBS and incubated with secondary antibodies at room temperature for 1 hour in blocking buffer. Cells were again washed 3 times with DPBS and then incubated with 1.67 μM DAPI (Millipore Sigma, Cat. No. D8417) or 6.67 μ M Hoechst (Thermo Scientific, Cat. No. 33342) for 5 minutes at room temperature. Cells were finally washed 3 times with DPBS, and the slide was mounted with ProLong™ Glass Antifade Mountant (Thermofisher, Cat. No. P36984). The slides were left to dry at room temperature overnight, protected from light. Alternatively, cells were kept in DPBS and imaged.

Lipidomics

iRPE cultured on Matrigel-coated 60 mm dishes were harvested using TrypLE™ (Thermo Scientific, Cat. No. 12563011). After creating a single-cell suspension, samples were mixed 1:1 with Trypan Blue (HiMedia, Cat. No. TCL005-100ml) and counted using the Countess 3

(Thermo Scientific, Cat. No. AMQAX2000). Cells were then centrifuged at 400 g for 5 minutes, and the resulting pellets were resuspended in 100 µL of molecular grade water. Gas and liquid chromatography-mass spectrometry were performed by the Peroxisomal Diseases Laboratory at the Kennedy Krieger Institute in Baltimore, MD, USA. Lipid fatty acids were acid hydrolyzed from triglycerides and phospholipids then measured as their pentafluorobenzyl bromide esters by isotope dilution capillary gas chromatography negative chemical ion GC-MS according to the method of Lagerstedt et al 2001[11]. Acylcarnitines and phosphatidylethanolamine plasmalogens were methanol extracted and analyzed by LC-MS/MS on an AB Sciex API3200 with either a Phenomenex Kinetex C8 column (2.6µm x 50 x 2.1 mm) using a linear gradient between 0.1% formic acid in H2O and 0.1% formic acid in methanol in positive electrospray ionization mode according to the method van de Beek 2016[12] or a Phenomenex Kinetex HILIC column (2.6µm x 30 x 3 mm) column using a linear gradient between 0.2% formic acid in 60mM ammonium formate and 0.2% formic acid in acetonitrile according to modified methods of De Biase et al., 2023[13] and Scherer et al., 2010[14].

Bovine Photoreceptor Outer Segments

Isolated bovine photoreceptor outer segments (POS) were acquired from InVision BioResources (22/2/2024 lot). POS pellets were gently resuspended in 10 mL of 8.3 pH wash buffer containing 20 g of sucrose (Fisher Scientific, Cat. No. BP2201) and 1.68 g of sodium bicarbonate (Fisher Scientific, Cat. No. BP3281), dissolved in a total volume of 200 mL Milli-Q water (Millipore Sigma). The resuspended POS were centrifuged at 600 g for 20 minutes at 4 °C. The resulting pellet was resuspended in 10 mL of wash buffer. Aliquots were mixed 1:1 with RIPA buffer (Thermo Scientific, Cat. No. 89900) supplemented with cOmplete™ Protease Inhibitor Cocktail

(Sigma Aldrich, Cat. No. 11697498001) for determining the protein concentration using Pierce™ BCA Protein Assay Kit (Thermo Scientific, Cat. No. 23225). For use in immunoblotting experiments, approximately 0.5 POS per cell was delivered in RPE-MM supplemented with 4 μ g/mL human protein S (Sino Biologicals, Cat. No. 12179-H08H-100) and 1.5 μg/mL human MFG-E8 (Sino Biologicals, Cat. No. 10853-H08B-1).

Flow Cytometry

Suitable gating strategies and other technical aspects of flow cytometry were developed in consultation with the University of Alberta Flow Cytometry Core Facility. A minimum of 10,000 events were captured for each sample on the flow cytometer. Cells were gated based on the FSC/SSC (forward scatter/ side scatter) profile to exclude debris and cell clumps. FSC area versus FSC height was then used to remove doublets. Single cells were gated based on fluorescence minus one (FMO) controls. Data including median fluorescence intensities were analyzed using FlowJo v10.10.0 (BD Biosciences).

Assessing Expression of Signature RPE Proteins: iRPE were harvested using TrypLE™ then fixed with 4% paraformaldehyde. The cells were washed with flow cytometry buffer (DPBS supplemented with 2% fetal bovine serum (Sigma Aldrich, Cat. No. F1051-500ml)) between steps. To permeabilize cells, 0.2% Triton X-100 (Bio-Rad, Cat. No. 1610407) was added to the flow cytometry buffer. Antibodies were incubated overnight at 4 °C on a rocker. The next day, cells were washed and incubated in secondary antibodies with the permeabilization buffer for 30 minutes at room temperature. The cells were then incubated in the flow cytometry buffer containing 1.67 μM DAPI (Millipore Sigma, Cat. No. D8417) for 5 minutes at room

temperature. After washes, the cells were finally resuspended in the flow cytometry buffer. Ten thousand events per sample were acquired on a 5-laser Cytek Aurora spectral flow cytometer (RRID:SCR_019826, Cytek Biosciences, Fremont, CA, USA) running SpectroFlo 3.1.0 with following panels: DAPI, MITF Alexa Fluor 488, BEST1 Alexa Fluor 546, and PMEL17 Alexa Fluor 647; or DAPI, PAX6 Alexa Fluor 488 and TYRP1 Alexa Fluor 647. Threshold was on FSC (50,000) in both cases.

Measuring Intracellular Neutral Lipids: iRPE were harvested using trypsin (Thermo Scientific, Cat. No. 25200072). Live cells were resuspended in DPBS and incubated with 2 µM Calcein (Thermo Scientific, Cat. No. L32250) for 30 minutes at room temperature, followed by a 5-minute incubation of 10 µM Hoechst (Thermo Scientific, Cat. No. 33342). LipidTOX Deep Red neutral lipid stain (Fisher Scientific, Cat. No. H34477) (1:100 dilution in DPBS) median fluorescent intensity was used to measure intracellular neutral lipid accumulation. At least 100,000 total events were acquired using an Attune NxT Acoustic Focusing Cytometer (RRID:SCR_019590, ThermoFisher Scientific, Burlington, ON, Canada) equipped with 4 lasers employing the indicated bandpass filters: 405 nm VL1 440/50 for Hoechst, 488 nm BL1 530/30 for Calcein, 561 nm YL1585/16 for pHrodo, and 634 nm RL1 670/14 for LipidTOX Deep Red. Compensation was applied among fluorochromes. Threshold was on FSC (25,000). Voltages used were FSC-A 70 V, SSC-A 280 V, BL1-A 220 V, YL1-A 250 V, RL1-A 220 V, and VL1-A 220 V.

Transepithelial Electrical Resistance

The EVOM3 (World Precision Instruments) was used to measure the transepithelial electrical resistance (TEER) of iRPE cultured on Matrigel-coated transwells (Corning, Cat. No. 3470) at baseline and following 150 µM palmitate treatment or a 24-hour POS (10 POS/cell) challenge.

Analysis Software

To quantify PMP70 positive puncta, captured z-stacks were analysed using IMARIS (Oxford Instruments, V. 10.1). The spots detection tool was employed with a 0.3 µm diameter parameter to automatically detect PMP70 positive puncta. Cell borders were manually drawn using the draw tool. The filter tool was used to determine the number of spots inside each cell by selecting all spots that were less than 0 µm away from the cell's three-dimensional surface. Data was managed using Microsoft® Excel® (Version 2401 Build 16.0.17231.20236). Maximum intensity projections were developed using ImageJ (NIH, V1.53t). Statistical analysis and graphing were performed in GraphPad Prism version 10.6.0. Illustrations were created using BioRender or Microsoft® PowerPoint® (Version 2512 Build 16.0.19530.20184).

Results

PEX1$_{-/-}$and *PEX6*$_{-/-}$iRPE Exhibit Properties of Mature RPE

To study the consequences of impaired peroxisome function in human RPE, *PEX1*$_{-/-}$, *PEX6*$_{-/-}$, and isogenic wildtype iPSCs were concurrently differentiated into RPE (Figure 1A). All three

iRPE lines achieved differentiation milestones (RPE progenitor, committed RPE, immature RPE, and mature RPE) at similar time points based on daily manual inspection with light microscopy throughout differentiation. At the mature RPE stage, all three iRPE lines expressed proteins consistent with differentiated RPE, including TYRP1, PAX6, PMEL17, BEST1, and MITF (Figure 1B) quantified by flow cytometry. In addition, there were no differences in the proportion of cells expressing RPE signature proteins across iRPE lines. All three iRPE lines developed pigment (Supplementary Figures 2A and B) and were observed to have small regions in the RPE monolayer with focal detachment from the culture surface (Supplementary Figure 2C). This latter phenomenon is due to the intrinsic fluid-pumping ability of the RPE, and is consistent with effective RPE polarization. [15,16] In addition, all three iRPE lines formed zona occludins-1-positive tight junctions evident by immunofluorescence microscopy (Figure 1C). There were no morphological differences between the three iRPE lines in terms of cell area or number of neighboring cells using REShAPE,[17] (Figures 1D and E) and the iRPE cell area was consistent with human RPE cell area *in vivo*. [18] Finally, all three iRPE lines achieved comparable transepithelial electrical resistance (TEER) (Figure 1F).

PEX1$_{-/-}$and *PEX6*$_{-/-}$iRPE Have Defective Import of Peroxisome Matrix Proteins

Knockout of PEX1 and PEX6 was confirmed by immunoblot using *PEX1*$_{-/-}$ and *PEX6*$_{-/-}$ iRPE lysates, respectively (Figures 2A and B). In addition, *PEX6*$_{-/-}$ iRPE had reduced PEX1 protein compared to wildtype iRPE, and PEX6 protein was not detected in *PEX1*$_{-/-}$ iRPE. PEX1 and PEX6 are tethered to the peroxisome membrane by PEX26 and facilitate the import of PTS1and PTS2-containing cargo into the peroxisome matrix by enabling the recycling of the cargos' cytosolic receptor, PEX5. Both PEX26 and PEX5 abundance were reduced in *PEX1*$_{-/-}$and *PEX6*$_{-/-}$

iRPE compared to wildtype iRPE (Figures 2C and D). There was no significant difference in the number of peroxisomes per cell across all three iRPE lines assessed by quantifying peroxisomal membrane protein-70 (PMP70) abundance using immunoblotting and fluorescence microscopy (Figures 2E, F, and G).

To assess the integrity of peroxisome matrix protein import, *PEX1*$_{-/-}$, *PEX6*$_{-/-}$, and wildtype iPSCs were transfected with a GFP-PTS1 reporter (GFP-SKL). For this experiment, iPSCs were studied given their substantially higher transfection efficiency compared to post-mitotic iRPE. [19] Forty-eight hours post-transfection, wildtype iPSCs displayed numerous intracellular GFP-PTS1positive puncta, suggesting successful trafficking of GFP to peroxisomes (Figure 3A). However, both transfected *PEX1*$_{-/-}$and *PEX6*$_{-/-}$ iPSCs demonstrated a diffuse cytosolic pattern of GFP fluorescence with no discernible GFP-PTS1-positive puncta, suggesting impaired GFP trafficking to peroxisomes (Figure 3A). The integrity of PTS1- and PTS2-mediated peroxisome matrix protein import was also assessed in iRPE by interrogating the proteolytic processing of peroxisomal β-oxidation enzymes, ACOX1, MFP2, and ACAA1 on an immunoblot. ACOX1 encodes acyl-CoA oxidase-1 and catalyzes the first and rate-limiting step of peroxisomal β-oxidation. [20,21] ACOX1 is a 72-kDa protein and contains a C-terminal PTS1 sequence that targets the protein to the peroxisome. Once imported into the peroxisome matrix, ACOX1 undergoes proteolytic cleavage by the peroxisomal protease, TYSND1, into active 50-kDa and 22-kDa fragments. [22] Wildtype iRPE, but not *PEX1*$_{-/-}$and *PEX6*$_{-/-}$ iRPE, demonstrated a prominent 22-kDa ACOX1 band on immunoblot, suggesting impaired PTS1-mediated peroxisome matrix protein import in *PEX1*$_{-/-}$and *PEX6*$_{-/-}$ iRPE (Figures 3B and C). *MFP2* encodes multifunctional protein-2, an enzyme that catalyzes the second and third steps of peroxisomal β-oxidation. [23] Similarly, once inside the peroxisome lumen, MFP2 is cleaved into an active form by TYSND1.[22] Only wildtype

iRPE demonstrated a prominent 45-kDa MFP2 band, representing the cleaved/processed form of the enzyme (Figures 3D and E). ACAA1 encodes acetyl-CoA acyltransferase-1 and catalyzes the final step of peroxisomal β-oxidation. [24,25]. ACAA1 is a 44-kDa protein that contains an N-terminal PTS2 sequence that is enzymatically cleaved in the peroxisome matrix by TYSND1.[22] Similar to the ACOX1 and MFP2 results, wildtype iRPE, but not *PEX1*$_{-/-}$ and *PEX6*$_{-/-}$ iRPE, demonstrated a cleaved form of ACAA1 on immunoblot, suggesting impaired PTS2-mediated peroxisome matrix protein import in *PEX1*$_{-/-}$ and *PEX6*$_{-/-}$ iRPE (Figures 3F and G).

Lipidomic Profiles of *PEX1*$_{-/-}$ and *PEX6*$_{-/-}$ iRPE Reveal Biochemical Abnormalities in PBDs

We performed lipidomic profiling of the three iRPE lines (n=3 replicates) using both gas and liquid chromatography-mass spectrometry approaches to elucidate specific lipid metabolic perturbations in iRPE with dysfunctional peroxisomes. Since plasmalogen synthesis requires functional peroxisomes, we measured phosphoethanolamine (PE)-containing plasmalogens,.[26] Both *PEX1*$_{-/-}$ and *PEX6*$_{-/-}$ iRPE had reduced levels for all PE-plasmalogen species measured, C18:0(plasm)-Total-PE displayed 8.8-fold decrease (p=2.1x10^{-8}) and 9.9-fold decrease (p=1.7x10^{-8}), respectively compared to wildtype iRPE (Figure 4A).

Clinically, VLCFAs are used as a biomarker for peroxisomal disorders[27]. *PEX1*$_{-/-}$ and *PEX6*$_{-/-}$ iRPE had significantly increased C26:0 compared to wildtype (24-fold increase; p=0.00048 and 17-fold increase; p=0.00027, respectively), dramatically increased C26:1ω9 (34-fold increase; p=0.0076 and 29-fold increase; p=0.000033, respectively), mildly increased C24:0 (1.4-fold increase; p=0.12 and 1.2-fold increase; p=0.15, respectively) and mildly decreased C22:0 (1.2-

fold decrease; p=0.23 and 1.3-fold decrease; p=0.029, respectively) (Figure 4B). There were no significant differences in VLCFAs levels between *PEX1*$_{-/-}$and *PEX6*$_{-/-}$iRPE. The long-chain FAs C16:0 and C18:0 were approximately one order of magnitude more abundant than the VLCFA species in iRPE. There were no significant differences in C16:0 and C18:0 levels across all three iRPE lines (Figure 4B). Compared to wildtype, the ratio of C26:0 to C22:0, a biochemical diagnostic test for patients with PBDs, was 27-fold higher in *PEX1*$_{-/-}$iRPE and 19-fold higher in *PEX6*$_{-/-}$iRPE. Similarly, the ratio of C24:0 to C22:0, another biochemical PBD test, was 1.8-fold higher in *PEX1*$_{-/-}$iRPE and 1.5-fold higher in *PEX6*$_{-/-}$iRPE compared to wildtype. Additionally, long chain acylcarnitine species were elevated in *PEX1*$_{-/-}$and *PEX6*$_{-/-}$iRPE relative to wildtype. Specifically, C26:0 acylcarnitine species were 7.0-fold higher (p=0.00042) in *PEX1*$_{-/-}$iRPE and 3.7-fold higher (p=0.12) in *PEX6*$_{-/-}$iRPE (Figure 4C).

The branched-chain fatty acids (BCFAs) pristanic acid and phytanic acid require intact [28,29] For peroxisome function for their metabolism by β-oxidation and α-oxidation, respectively. pristanic acid, in comparison to wildtype iRPE, *PEX1*$_{-/-}$iRPE had a 96.9-fold increased level (p=0.0029) and *PEX6*$_{-/-}$iRPE had a 94.4-fold increased level (p=0.00053). For phytanic acid, relative to wildtype iRPE, *PEX1*$_{-/-}$iRPE had a 13.2-fold increased level (p=0.0044) and *PEX6*$_{-/-}$iRPE had a 11.6-fold increased level (p=0.00060). There were no significant differences in BCFA levels between *PEX1*$_{-/-}$and *PEX6*$_{-/-}$ iRPE (Figure 4D).

Intracellular Lipid Accumulates in *PEX1*$_{-/-}$and *PEX6*$_{-/-}$iRPE

Given the essential role of peroxisomes in lipid metabolism, we investigated whether intracellular lipids accumulate in *PEX1*$_{-/-}$and *PEX6*$_{-/-}$iRPE relative to wildtype iRPE. *PEX1*$_{-/-}$iRPE had a 1.6-fold greater LipidTOX Deep Red median fluorescence intensity (MFI) relative to

wildtype iRPE measured by flow cytometry, indicating increased intracellular neutral lipids (p=0.042). Similarly, *PEX6*$^{-/-}$iRPE had a 1.9-fold greater LipidTOX Deep Red MFI relative to wildtype iRPE (p=0.017), suggesting increased intracellular neutral lipids (Figure 5A). Both immunofluorescence microscopy and immunoblotting using antibodies against perilipin-2 (PLIN2), one of the most abundant lipid droplet (LD)-related proteins, [30] revealed increased PLIN2 in *PEX1*$^{-/-}$and *PEX6*$^{-/-}$iRPE relative to wildtype at baseline (Figures 5B, C, and D). By immunoblot analysis, *PEX1*$^{-/-}$and *PEX6*$^{-/-}$ iRPE had 1.8-fold (p=0.017) and 2.3-fold (p=0.0016) increases in PLIN2, respectively, compared to wildtype iRPE at baseline (Figures 5B and D). Next, all three iRPE lines were subjected to a 1, 12, or 24-hour continuous POS challenge (0.5 POS per cell). After the 1-hour POS challenge, PLIN2 increased in wildtype, *PEX1*$^{-/-}$and *PEX6*$^{-/-}$iRPE. However, relative to PLIN2 levels at 1 hour, wildtype iRPE demonstrated a 34% reduction in PLIN2 at 12 hours, whereas *PEX1*$^{-/-}$and *PEX6*$^{-/-}$iRPE demonstrated only 13% and 11% reductions in PLIN2 at 12 hours, respectively. At 24 hours, PLIN2 levels remained persistently higher in the *PEX1*$^{-/-}$(1.9-fold increase; p=0.047) and *PEX6*$^{-/-}$iRPE (2.5-fold increase; p=0.024) relative to wildtype (Figures 5D and E).

<u>*PEX1*$^{-/-}$ and *PEX6*$^{-/-}$iRPE Have Reduced DHA and Impaired Retroconversion of ω3 and ω6 PUFAs</u>

To evaluate the effect of peroxisome dysfunction on the metabolism of specific lipid species present in POS, we measured the lipid profiles of the three iRPE lines before and after a POS challenge using GC-MS. First, we identified and quantified the FA lipid species present in isolated bovine POS. The most abundant PUFA lipid species was DHA (C22:6ω3) at 151.8 pmol/μg of total protein, representing 36.6% of all measured FA lipid species (Figure 6A).

The second and third most abundant PUFAs were C22:5ω6 (DPAω6) (41.5 pmol/μg of total protein) and C20:4ω6 (AA) (26.3 pmol/μg of total protein), respectively. EPA (C20:5ω3) existed in only trace amounts in bovine POS. The most abundant saturated FA lipid species were C18:0 (99.8 pmol/μg of total protein) and C16:0 (75.4 pmol/μg of total protein) (Figure 6A). A comprehensive dataset of measured lipid species in bovine POS is available in Supplementary Table 2.

The ω3 PUFAs are essential lipids since they cannot be synthesized *de novo* in humans, yet they are highly abundant in the brain and retina[31] . These lipids have critical roles in POS membrane structure and support phototransduction, and they impart cellular anti-inflammatory, anti-oxidative, and neuroprotective properties. [32] The biosynthesis of ω3 PUFAs begins with dietary α-linolenic acid (ALA; C18:3ω3) and proceeds through a series of elongation and desaturation reactions to generate EPA (C20:5ω3) and DHA (C22:6ω3). Both DHA and its precursor, C24:6ω3, can be retroconverted to EPA through a series of β-oxidation steps that occur in peroxisomes (Figure 6C).[33] The relative contribution of the retroconversion pathway for generating intracellular EPA pools has been debated, and it has not been studied in the RPE in the context of peroxisome dysfunction. [34–36] To address this, we measured ω3 PUFAs before and after a 7-day POS challenge (3 POS per iRPE cell were added with daily media changes) in all three iRPE lines.

At baseline, *PEX1*$_{-/-}$and *PEX6*$_{-/-}$iRPE had significantly elevated ALA relative to wildtype iRPE (2.2-fold increase (p=0.011) and 2.1-fold increase (p=0.0047), respectively). In contrast, *PEX1*$_{-/}$and *PEX6*$_{-/-}$iRPE had significantly reduced EPA (1.8-fold decrease (p=0.010) and 1.8-fold decrease (p=0.0020), respectively) and DHA (3.1-fold decrease (p=0.00050) and 4.2-fold decrease (p=0.000079), respectively) relative to wildtype iRPE (Figure 6B). Following the POS

challenge, DHA significantly increased across all iRPE lines relative to baseline (wildtype: 2.4fold increase (p=0.00011), *PEX1*$_{-/-}$: 6.5-fold increase (p=0.0017), and *PEX6*$_{-/-}$: 8.1-fold increase (p=0.00038)). Despite only trace amounts of EPA (and other ω3 species except DHA) in bovine POS, there was a 1.7-fold increase (p=0.000093) in EPA, the retroconversion product of DHA, post-POS challenge in wildtype iRPE. In stark contrast, *PEX1*$_{-/-}$and *PEX6*$_{-/-}$iRPE did not demonstrate an increase in EPA following the POS challenge (p=0.76 and p=0.49, respectively) (Figure 6B). To determine whether the increase in EPA in wildtype iRPE, but not *PEX1*$_{-/-}$and *PEX6*$_{-/-}$iRPE, was from the DHA in POS, we challenged all three iRPE lines with 30 uM DHA conjugated to BSA. We observed the same result as the POS challenge, suggesting impaired DHA retroconversion in *PEX1*$_{-/-}$and *PEX6*$_{-/-}$iRPE (Supplementary Figures 3A and B).

We simultaneously evaluated changes in the ω6 PUFA species in all three iRPE lines before and after a POS challenge. The metabolic pathway for the ω6 PUFAs mirrors that of the ω3 PUFAs, and they compete for the same set of enzymes (Figure 6E).[37] Consistent with the ω3 PUFAs results, following the POS challenge, all three iRPE lines accumulated C22:5ω6 (DPAω6), which is the most common of the ω6 PUFA detected in bovine POS and is the ω6 PUFA equivalent of DHA (wildtype: 7.6-fold increase (p=0.000081), *PEX1*$_{-/-}$: 12.2-fold increase (p=0.0018), and *PEX6*$_{-/-}$: 14.4-fold increase (p=0.00027) (Figure 6D). However, the *PEX1*$_{-/-}$and *PEX6*$_{-/-}$iRPE accumulated approximately twice the amount of C22:5ω6 relative to wildtype iRPE following the POS challenge (p=0.019 and p=0.0033, respectively). In addition, wildtype iRPE had a 1.3fold increase (p=0.013) in arachidonic acid (C20:4ω6), the ω6 PUFA equivalent of EPA and retroconversion product of C22:5ω6, following a POS challenge. Both *PEX1*$_{-/-}$and *PEX6*$_{-/-}$iRPE failed to significantly accumulate C20:4ω6 following a POS challenge (p=0.63 and p=0.055, respectively) (Figure 6D). Similar to the ω3 PUFA species, we challenged all three iRPE lines

with 30 uM DPAω6 conjugated to BSA and observed the same result as the POS challenge, suggesting impaired DPAω6 retroconversion in *PEX1*$_{-/-}$and *PEX6*$_{-/-}$iRPE (Supplementary Figures 3C and D).

PEX1$^{-/-}$ and *PEX6*$^{-/-}$ iRPE Have Disrupted Phagocytosis of Photoreceptor Outer Segments

Emerging evidence suggests a critical role of peroxisomes in phagocytosis, especially for immune cells. [38,39] To determine the consequence of peroxisome dysfunction on phagocytosis in the RPE, the presence of rhodopsin, a protein that is not expressed in the RPE but is the most abundant protein in POS, was evaluated using an antibody recognizing an epitope on the N-terminus of the protein. Since alterations in phagocytosis may be attributed to differences in POS uptake, degradation, or a combination of both, we utilized an approach that more broadly measures total POS consumption by the RPE called the total RPE consumption capacity.[40] This assay measures the amount of POS persisting both inside the RPE (engulfed but not degraded) and within the media (not engulfed) by rhodopsin immunoblotting of harvested cells and media together after a continuous POS challenge. [40] . Following a 1-hour POS challenge, there was no significant difference between total rhodopsin (iRPE lysates and media) in wildtype, *PEX1*$_{-/-}$or *PEX6*$_{-/-}$iRPE (Figures 7A and B). However, by 24 hours, wildtype iRPE had the largest reduction in rhodopsin, with only 19.5% of initial rhodopsin remaining, compared to 31.9% and 34.9% of initial rhodopsin remaining in *PEX1*$_{-/-}$and *PEX6*$_{-/-}$iRPE, respectively. By 24 hours, *PEX1*$_{-/-}$and *PEX6*$_{-/-}$iRPE had 1.7-fold higher (p=0.022) and 1.9-fold higher (p=0.0073) levels of rhodopsin relative to wildtype respectively, suggesting impaired rhodopsin degradation and disrupted POS phagocytosis in *PEX1*$_{-/-}$and *PEX6*$_{-/-}$iRPE (Figures 7A and B).

Finally, we measured transepithelial electrical resistance (TEER) of the iRPE lines following a 24-hour POS challenge. Incubating the iRPE for 24 hours with 150 μM of palmitate, a lipotoxic concentration of the fatty acid that reduces cellular metabolic activity,[41] resulted in an approximately 2-fold reduction in TEER from baseline that did not significantly differ across all three iRPE lines (Figure 7C). Following a 24-hour POS challenge, there was no change in TEER in wildtype iRPE compared to baseline. However, following a 24-hour POS challenge, *PEX1*$_{-/-}$iRPE had a 2.5-fold reduction in TEER compared to baseline (p=1.1E-8). Similarly, *PEX6*$_{-/-}$ iRPE had a 2.2-fold reduction in TEER following a 24-hour POS challenge compared to baseline (p=4.4E-8) (Figure 7C). Together, our data suggest that *PEX1*$_{-/-}$and *PEX6*$_{-/-}$ iRPE have altered phagocytosis evident by the disrupted processing of POS containing rhodopsin, which results in a reduction in RPE cellular health, as assessed by TEER.

Discussion

We have developed the first human iPSC-derived RPE models to study the effects of peroxisome [42,43] The dysfunction in the RPE, an essential retinal layer that is disrupted in patients with PBDs. *PEX1*$_{-/-}$and *PEX6*$_{-/-}$ iRPE recapitulated features of differentiated RPE as demonstrated by the development of pigmentation, hexagonal morphology with tight junctions, transepithelial electrical resistance, and expression of RPE signature proteins (Figure 1). These properties closely resemble those of other iRPE models and cultured primary human RPE. [44–46] We did not appreciate any differences in the development of these RPE features when comparing *PEX1*$_{-/-}$and *PEX6*$_{-/-}$ iRPE to wildtype iRPE, suggesting that intact peroxisome function may not be essential for iPSC generation and RPE maturation *in vitro*. Wang and colleagues differentiated

iPSCs from patients with *PEX1*-, *10*-, *12*-, and *26*-related PBDs into neurons and reported a 1.8fold reduction in the efficiency of neural rosette formation from embryoid bodies (EBs) in the PDB cohort compared to controls. [47] However, iPSCs derived from the PBD cohort could differentiate into neurons with measurable electrophysiological responses. On the other hand, the authors reported morphological variations in differentiated oligodendrocytes where those derived from a patient with a *PEX1*-related PBD had an attenuated branching pattern. [47] In contrast, Pellegrino *et al.* (2023) generated *PEX3*$^{-/-}$iPSC-derived macrophages and reported no significant effect of *PEX3* deletion on differentiation. [48] Considering these observations, the requirement of intact peroxisome function for cellular differentiation may be cell- or tissue-specific, and there may exist mechanisms to compensate for reduced peroxisome activity during differentiation.

Alternating subunits of PEX1 and PEX6 proteins assemble as a heterohexamer and are anchored to the peroxisome membrane by PEX26. Together, these proteins function as the peroxisome exportomer complex and facilitate the ATP-dependent release of the cytosolic receptor, PEX5, for subsequent rounds of matrix protein import. [49] Biallelic pathogenic variants in *PEX1* and *PEX6* result in disrupted import of peroxisome matrix proteins. [1] As expected, the *PEX1*$^{-/-}$and *PEX6*$^{-/-}$ iRPE demonstrated impaired proteolytic processing of ACOX1, MFP2, and ACAA1, suggesting that these enzymes did not effectively reach the peroxisome matrix where they are normally cleaved (Figure 3). [22] Moreover, GFP-tagged SKL, the C-terminal PTS1 tripeptide that targets proteins to the peroxisome matrix, was mislocalized to the cytosol in *PEX1*$^{-/-}$and *PEX6*$^{-/-}$ iPSCs, confirming a global defect in matrix protein import (Figure 3). Consistent with studies in fibroblasts from patients with *PEX1*-, *PEX6*-, and *PEX26*-related PBDs demonstrating reduced [50,51] the *PEX1*$^{-/-}$PEX5 protein abundance, and *PEX6*$^{-/-}$ iRPE also had decreased PEX5 protein

compared to wildtype iRPE (Figure 2), likely due to a quality control mechanism that reduces the accumulation of inoperable PEX5 on peroxisome membranes. [52] Interestingly, knockout of either PEX1 or PEX6 reduced the abundance of the other protein, an effect especially pronounced in *PEX6*$^{-/-}$ iRPE where PEX1 was not detectable (Figure 2). This finding is in agreement with a recent study that demonstrated reduced PEX1 when PEX6 was knocked-down in HCT116 cells, [53] and likely occurs due to the process by which cells degrade unpaired subunits in protein complexes.[54]

While the import of matrix proteins was impaired in *PEX1*$^{-/-}$and *PEX6*$^{-/-}$ iRPE, the number of peroxisomes per cell was not significantly different from wildtype iRPE (Figure 2). This differs from the reduced peroxisome abundance reported in *PEX6*$^{-/-}$ HEK293T cells[42] and *PEX1*$^{-/}$patient fibroblasts, [55] where the latter study mechanistically linked reduced peroxisome abundance to increased peroxisome degradation by pexophagy. [55] We suspect that the effect of *PEX1* and *PEX6* mutation on peroxisome abundance could be cell-type specific, and the highly metabolically active RPE may upregulate peroxisome biogenesis in an attempt to offset peroxisome degradation and dysfunction. Given the remarkable ability of peroxisomes to change in size, number, morphology, and enzyme content in response to environmental stimuli, [56] it is possible that peroxisome dynamics change in the RPE under physiological stressors such as POS phagocytosis.

Lipid biochemical analyses of iRPE confirmed significantly elevated VLCFAs, BCFAs, and reduced plasmalogens in *PEX1*$^{-/-}$and *PEX6*$^{-/-}$ iRPE compared to wildtype iRPE (Figure 4),

recapitulating lipid abnormalities in both plasma and dermal fibroblasts from patients with severe PBDs[57–59] and in the RPE of *Pex1*-p.G844D mutant mice.[60] Elevated VLCFAs implies impaired peroxisomal β-oxidation in *PEX1*$_{-/-}$ and *PEX6*$_{-/-}$ iRPE, consistent with the perturbed proteolytic processing of ACOX1, MFP2, and ACAA1, three essential enzymes in peroxisomal β-oxidation (Figure 3). Intriguingly, the *PEX1*$_{-/-}$ and *PEX6*$_{-/-}$ iRPE each demonstrated a nearly 100-fold increase in pristanic acid and more than 10-fold increase in phytanic acid compared to wildtype iRPE, despite the relatively low abundance of these BCFAs in FBS-containing media.[61] Patients[57,59] with PBDs typically do not demonstrate such a profound increase in BCFAs in their plasma. The accumulation of phytanic acid and pristanic acid in *PEX1*$_{-/-}$ and *PEX6*$_{-/-}$ iRPE may contribute to the retinal degeneration phenotype in patients with PBDs. In support of this hypothesis, patients with adult Refsum disease accumulate massive amounts of phytanic acid due to loss-of-function of the peroxisomal enzyme phytanoyl-CoA hydroxylase and develop retinal degeneration that resembles that seen in patients with PBDs.[62] Both pristanic acid and phytanic acid induce mitochondrial dysfunction and disrupt calcium homeostasis in rat neurons and glia.[63] In primary human RPE, phytanic acid accumulation leads to ultrastructural disturbances including vacuolation and loss of apical microvilli.[64] Whereas the progression of retinal degeneration in patients with adult Refsum disease can be slowed by dietary restriction of phytanic acid,[62] it is unknown whether this occurs in patients with PBDs.

One of the major roles of the RPE in maintaining normal vision is the continuous phagocytosis and metabolism of POS. The POS are enriched in very long-chain-PUFAs (VLC-PUFAs) and various long-chain PUFAs (LC-PUFAs), including DHA, and their daily phagocytosis places a large metabolic burden on the RPE.[65] We identified an accumulation of LipidTOX Deep Red-

positive intracellular neutral lipids in *PEX1*$_{-/-}$and *PEX6*$_{-/-}$ iRPE compared to wildtype iRPE at baseline, which correlated with PLIN2-positive lipid droplet formation (Figure 5). Since peroxisomes import and oxidize fatty acids released from lipid droplets, [66] differences in neutral lipid accumulation in *PEX1*$_{-/-}$and *PEX6*$_{-/-}$ iRPE compared to wildtype iRPE at baseline could be due to compromised peroxisome-lipid droplet interactions. [67] Following a POS challenge in *PEX1*$_{-/-}$and *PEX6*$_{-/-}$ iRPE, fatty acids that would normally be metabolized by peroxisomes may instead accumulate in the RPE and become esterified and subsequently stored in lipid droplets.

In addition, a reduced total RPE consumption capacity for rhodopsin was observed in *PEX1*$_{-/-}$and *PEX6*$_{-/-}$ iRPE compared to wildtype, and a reduction in RPE cellular health demonstrated by reduced TEER in *PEX1*$_{-/-}$and *PEX6*$_{-/-}$ iRPE (Figure 7). Peroxisomal phosphatidylinositol 4,5bisphosphate (PI(4,5)P2) and lysosomal synaptotagmin VII interact to establish membrane contact sites and facilitate the transfer of cholesterol from lysosomes to peroxisomes. [68] Given that *PEX1* and *PEX6* knockdown in HeLa cells reduces peroxisomal PI(4,5)P2, and cholesterol accumulates in PBD patient fibroblasts, [68] *PEX1*$_{-/-}$and *PEX6*$_{-/-}$ iRPE may also have disrupted peroxisome-lysosome interactions leading to lipid accumulation and lysosomal dysfunction. Kocherlakota and colleagues identified lipid droplet accumulation and lysosomal dysfunction in the RPE of both global and RPE-specific *Mfp2*$_{-/-}$mice, [4] supporting this hypothesis. Our iRPE models offer a platform to further investigate the coordination and regulation of peroxisomes, lipid droplets, and lysosomes in the RPE.

While RPE degeneration occurs in patients with biallelic pathogenic loss-of-function variants in *PEX1* and *PEX6*, [42,43] our *PEX1*$_{-/-}$and *PEX6*$_{-/-}$ iRPE did not demonstrate any overt signs of degeneration at baseline. However, when these iRPE were burdened with a physiological lipid load in the form of POS, both *PEX1*$_{-/-}$and *PEX6*$_{-/-}$ iRPE had a greater than 50% reduction in TEER, indicating disrupted integrity of the RPE barrier and reduced cellular health. [69] We hypothesize that the *PEX1*$_{-/-}$and *PEX6*$_{-/-}$ iRPE may have altered metabolic pathways that compensate for peroxisome dysfunction, but that these processes become overwhelmed during POS phagocytosis. Intriguingly, while an RPE-specific deletion of *Mfp2* led to RPE dysfunction and secondary photoreceptor degeneration in mice, RPE degeneration did not occur in *Mfp2*/*rd1* double mutants that do not develop POS. [4] Consistent with our *PEX1*$_{-/-}$and *PEX6*$_{-/-}$ iRPE, this implies that the RPE is highly dependent on β-oxidation reactions housed inside functional peroxisomes for POS phagocytosis.

DHA is the most abundant ω3 PUFA in the retina and modulates outer segment fluidity and supports phototransduction. [70,71] Peroxisomal β-oxidation is required to generate DHA through the retroconversion of C24:6ω3 (THA) to DHA, a pathway called Sprecher's shunt. [72–74] DHA can be further retroconverted to EPA, a process that also depends on intact peroxisomes, [75] and an analogous retroconversion pathway exists for ω6 PUFAs. [76] The physiological relevance of these pathways, however, is poorly understood. Boeck and colleagues reported substantially increased C22:5ω6 in the retinas of *Acox1*$_{-/-}$mice that was attributed to DHA deficiency, but the precise mechanism was difficult to ascertain. [77] Following a challenge with bovine POS with a defined fatty acid profile consistent with the published lipid composition of rod outer segments, [70,78] we identified an increase in ω3 and ω6 retroconversion products EPA (C20:5ω3) and AA (C20:4ω6),

respectively, in wildtype iRPE but not in *PEX1*$_{-/-}$and *PEX6*$_{-/-}$ iRPE (Figure 6). The accumulation of EPA and AA in wildtype iRPE occurred despite these fatty acids not being substantially abundant in POS. Moreover, wildtype iRPE, but not *PEX1*$_{-/-}$and *PEX6*$_{-/-}$ iRPE, accumulated EPA and AA when cultured with 30 μM DHA and 30 μM DPAω6 (C22:5ω6), respectively, indicating that the source of EPA and AA is likely from peroxisome-dependent retroconversion (Supplementary Figure 3). Consistent with *Acox1*$_{-/-}$murine retinas, we identified a significant increase in DPAω6, the second most abundant LC-PUFA in POS, in *PEX1*$_{-/-}$and *PEX6*$_{-/-}$ iRPE following a POS challenge (Figure 6). We conclude that impaired peroxisome-dependent retroconversion pathways are responsible for DPAω6 accumulation, rather than a deficiency of DHA *per se*. Precisely why the RPE prioritizes retroconverting DHA to EPA (and the ω6 PUFA equivalents) is unknown, but one explanation may be for the generation of retinal VLC-PUFAs, as EPA is the preferred substrate of ELOVL4, an elongase in photoreceptors. [76] Finally, while the *PEX1*$_{-/-}$and *PEX6*$_{-/-}$ iRPE had reduced DHA levels at baseline, following a POS challenge, wildtype, *PEX1*$_{-/-}$, and *PEX6*$_{-/-}$ iRPE all accumulated DHA to a similar level (Figure 6), suggesting that RPE may regulate or buffer specifically intracellular DHA levels, but further experiments are required to evaluate this possibility.

Our study has several limitations. First, the pigmentation of the iRPE limited our ability to acquire confocal microscopy images of our cells in a completely unbiased manner (i.e. capturing random fields of view). For example, for determining peroxisome abundance, we imaged iRPE where we could visualize PMP70-positive puncta, which was biased towards less pigmented cells that could differ physiologically from more pigmented iRPE. Second, we lacked a robust means of standardizing and comparing POS uptake precisely across our iRPE as the outer

segment fragments differed in size and thus lipid and protein amounts. Lastly, all of our iPSC lines had a chromosome 20q copy number gain (Supplementary Figure 4), a common iPSC karyotype abnormality that may confer a growth advantage in culture.[79]

In summary, our work has established the first human iRPE models to study the effects of peroxisome dysfunction in a disease-relevant cell type. *PEX1*$^{-/-}$and *PEX6*$^{-/-}$ iRPE develop normally, but demonstrate significant abnormalities following POS exposure, including impaired DHA retroconversion, reduced outer segment phagocytosis capacity, lipid droplet accumulation, and diminished TEER. Our findings suggest that peroxisomes in the RPE have a critical role in the metabolism of photoreceptor lipids, and disruption of this process may underlie retinal degeneration in patients with peroxisomal disorders.

Resource Availability

Lead Contact

Any requests for additional information or resources should be directed to the lead contact, Matthew D. Benson (mbenson@ualberta.ca).

Data and Code Availability

All data reported in this paper will be shared by the lead contact upon request.

Acknowledgments

The authors would like to thank all former and current members of the Benson lab. We thank Drs. Andrew Simmonds, Brittany Carr, Ian MacDonald, and Robin Clugston for their technical expertise, experimental advice, and sharing of reagents. We thank Dr. Davide Ortolan for sharing his expertise with REShAPE. Lai Xu and Dr. Gabrielle Siegers assisted with experiments performed at the University of Alberta Flow Cytometry Facility (RRID:SCR_019195, which receives financial support from the Faculty of Medicine & Dentistry (FoMD) and Canada Foundation for Innovation (CFI) awards to contributing investigators) and Cell Imaging Core (RRID:SCR_019200, which receives financial support from the FoMD, the University Hospital Foundation, Striving for Pandemic Preparedness – The Alberta Research Consortium, and CFI awards to contributing investigators). This research is funded by Fighting Blindness Canada (grant #RG2401). Acknowledgement is made to the donors of the Postdoctoral Fellowship Program in Macular Degeneration Research (MDR), grant # M2024001F, a program of the BrightFocus Foundation, for support of this research. J.M.L.M. is supported by the James Grosfield Initiative for Dry AMD, an RPB Career Development Award, and a National Eye Institute Career Development Award (K08EY033420). M.D.B. is supported by a Bayer Professorship in Translational Research in Ophthalmology.

Author Contributions

C.M. designed and conducted the experiments, analyzed the data, and drafted the original manuscript. C.B.F, S.H., J.H., E.T., Q.Z., A.R., H.H., B.C.H., E.M., and A.R. conducted experiments and analyzed the data. T.D.F., R.B.H., J.M.L.M., and M.D.B. conceptualized

experiments, developed methodology, and supervised research activities. M.D.B. reviewed and edited the manuscript and generated the final draft of the manuscript.

Declaration of Interests

The authors confirm that they have no relevant conflicts of interest.

References

1. Wanders, R.J.A., Baes, M., Ribeiro, D., Ferdinandusse, S., and Waterham, H.R. (2023). The physiological functions of human peroxisomes. Physiol. Rev. *103*, 957–1024. https://doi.org/10.1152/physrev.00051.2021.

2. Agbaga, M.-P., Mandal, M.N.A., and Anderson, R.E. (2010). Retinal very long-chain PUFAs: new insights from studies on ELOVL4 protein. J. Lipid Res. *51*, 1624–1642. https://doi.org/10.1194/jlr.R005025.

3. Daniele, L.L., Caughey, J., Volland, S., Sharp, R.C., Dhingra, A., Williams, D.S., Philp, N.J., and Boesze-Battaglia, K. (2019). Peroxisome turnover and diurnal modulation of antioxidant activity in retinal pigment epithelia utilizes microtubule-associated protein 1 light chain 3B (LC3B). Am. J. Physiol. Cell Physiol. *317*, C1194–C1204. https://doi.org/10.1152/ajpcell.00185.2019.

4. Kocherlakota, S., Das, Y., Swinkels, D., Vanmunster, M., Callens, M., Vinckier, S., Vaz, F.M., Sinha, D., Van Veldhoven, P.P., Fransen, M., et al. (2023). The murine retinal pigment epithelium requires peroxisomal β-oxidation to maintain lysosomal function and prevent dedifferentiation. Proc. Natl. Acad. Sci. *120*, e2301733120. https://doi.org/10.1073/pnas.2301733120.

5. Das, Y., Swinkels, D., Kocherlakota, S., Vinckier, S., Vaz, F.M., Wever, E., Van Kampen, A.H.C., Jun, B., Do, K.V., Moons, L., et al. (2021). Peroxisomal Multifunctional Protein 2 Deficiency Perturbs Lipid Homeostasis in the Retina and Causes Visual Dysfunction in Mice. Front. Cell Dev. Biol. *9*, 632930. https://doi.org/10.3389/fcell.2021.632930.

6. Argyriou, C., Polosa, A., Cecyre, B., Hsieh, M., Di Pietro, E., Cui, W., Bouchard, J.-F., Lachapelle, P., and Braverman, N. (2019). A longitudinal study of retinopathy in the PEX1-Gly844Asp mouse model for mild Zellweger Spectrum Disorder. Exp. Eye Res. *186*, 107713. https://doi.org/10.1016/j.exer.2019.107713.

7. Waterham, H.R., and Ebberink, M.S. (2012). Genetics and molecular basis of human peroxisome biogenesis disorders. Biochim. Biophys. Acta *1822*, 1430–1441. https://doi.org/10.1016/j.bbadis.2012.04.006.

8. Yergeau, C., Coussa, R.G., Antaki, F., Argyriou, C., Koenekoop, R.K., and Braverman, N.E. (2023). Zellweger Spectrum Disorder: Ophthalmic Findings from a New Natural History Study Cohort and Scoping Literature Review. Ophthalmology *130*, 1313–1326. https://doi.org/10.1016/j.ophtha.2023.07.026.

9. Sharma, R., Bose, D., Montford, J., Ortolan, D., and Bharti, K. (2022). Triphasic developmentally guided protocol to generate retinal pigment epithelium from induced pluripotent stem cells. STAR Protoc. *3*, 101582. https://doi.org/10.1016/j.xpro.2022.101582.

10. Regent, F., Morizur, L., Lesueur, L., Habeler, W., Plancheron, A., Ben M'Barek, K., and Monville, C. (2019). Automation of human pluripotent stem cell differentiation toward retinal pigment epithelial cells for large-scale productions. Sci. Rep. *9*, 10646. https://doi.org/10.1038/s41598-019-47123-6.

11. Lagerstedt, S.A., Hinrichs, D.R., Batt, S.M., Magera, M.J., Rinaldo, P., and McConnell, J.P. (2001). Quantitative Determination of Plasma C8–C26 Total Fatty Acids for the Biochemical Diagnosis of Nutritional and Metabolic Disorders. Mol. Genet. Metab. *73*, 38–45. https://doi.org/10.1006/mgme.2001.3170.

12. Van De Beek, M.-C., Dijkstra, I.M.E., Van Lenthe, H., Ofman, R., Goldhaber-Pasillas, D., Schauer, N., Schackmann, M., Engelen-Lee, J.-Y., Vaz, F.M., Kulik, W., et al. (2016). C26:0-Carnitine Is a New Biomarker for X-Linked Adrenoleukodystrophy in Mice and Man. PLOS ONE *11*, e0154597. https://doi.org/10.1371/journal.pone.0154597.

13. De Biase, I., Yuzyuk, T., Cui, W., Zuromski, L.M., Moser, A.B., and Braverman, N.E. (2023). Quantitative analysis of ethanolamine plasmalogen species in red blood cells using liquid chromatography tandem mass spectrometry for diagnosing peroxisome biogenesis disorders. Clin. Chim. Acta *542*, 117295. https://doi.org/10.1016/j.cca.2023.117295.

14. Scherer, M., Leuthäuser-Jaschinski, K., Ecker, J., Schmitz, G., and Liebisch, G. (2010). A rapid and quantitative LC-MS/MS method to profile sphingolipids. J. Lipid Res. *51*, 2001–2011. https://doi.org/10.1194/jlr.D005322.

15. Dvoriashyna, M., Foss, A.J.E., Gaffney, E.A., and Repetto, R. (2020). Fluid and solute transport across the retinal pigment epithelium: a theoretical model. J. R. Soc. Interface *17*, 20190735. https://doi.org/10.1098/rsif.2019.0735.

16. Shi, G., Maminishkis, A., Banzon, T., Jalickee, S., Li, R., Hammer, J., and Miller, S.S. (2008). Control of Chemokine Gradients by the Retinal Pigment Epithelium. Investig. Opthalmology Vis. Sci. *49*, 4620. https://doi.org/10.1167/iovs.08-1816.

17. Ortolan, D., Sharma, R., Volkov, A., Maminishkis, A., Hotaling, N.A., Huryn, L.A., Cukras, C., Di Marco, S., Bisti, S., and Bharti, K. (2022). Single-cell-resolution map of human retinal pigment epithelium helps discover subpopulations with differential disease sensitivity. Proc. Natl. Acad. Sci. U. S. A. *119*, e2117553119. https://doi.org/10.1073/pnas.2117553119.

18. Granger, C.E., Yang, Q., Song, H., Saito, K., Nozato, K., Latchney, L.R., Leonard, B.T., Chung, M.M., Williams, D.R., and Rossi, E.A. (2018). Human Retinal Pigment Epithelium: In Vivo Cell Morphometry, Multispectral Autofluorescence, and Relationship to Cone Mosaic. Invest. Ophthalmol. Vis. Sci. *59*, 5705–5716. https://doi.org/10.1167/iovs.18-24677.

19. Zabner, J., Fasbender, A.J., Moninger, T., Poellinger, K.A., and Welsh, M.J. (1995). Cellular and molecular barriers to gene transfer by a cationic lipid. J. Biol. Chem. *270*, 18997–19007. https://doi.org/10.1074/jbc.270.32.18997.

20. Ferdinandusse, S., Denis, S., Hogenhout, E.M., Koster, J., Van Roermund, C.W.T., IJlst, L., Moser, A.B., Wanders, R.J.A., and Waterham, H.R. (2007). Clinical, biochemical, and mutational spectrum of peroxisomal acyl–coenzyme A oxidase deficiency. Hum. Mutat. *28*, 904–912. https://doi.org/10.1002/humu.20535.

21. Oaxaca-Castillo, D., Andreoletti, P., Vluggens, A., Yu, S., Van Veldhoven, P.P., Reddy, J.K., and Cherkaoui-Malki, M. (2007). Biochemical characterization of two functional human liver acyl-CoA oxidase isoforms 1a and 1b encoded by a single gene. Biochem. Biophys. Res. Commun. *360*, 314–319. https://doi.org/10.1016/j.bbrc.2007.06.059.

22. Kurochkin, I.V., Mizuno, Y., Konagaya, A., Sakaki, Y., Schönbach, C., and Okazaki, Y. (2007). Novel peroxisomal protease Tysnd1 processes PTS1- and PTS2-containing enzymes involved in beta-oxidation of fatty acids. EMBO J. *26*, 835–845. https://doi.org/10.1038/sj.emboj.7601525.

23. Huyghe, S., Mannaerts, G.P., Baes, M., and Van Veldhoven, P.P. (2006). Peroxisomal multifunctional protein-2: The enzyme, the patients and the knockout mouse model. Biochim. Biophys. Acta BBA - Mol. Cell Biol. Lipids *1761*, 973–994. https://doi.org/10.1016/j.bbalip.2006.04.006.

24. Ferdinandusse, S., Denis, S., Mooijer, P.A., Zhang, Z., Reddy, J.K., Spector, A.A., and Wanders, R.J. (2001). Identification of the peroxisomal beta-oxidation enzymes involved in the biosynthesis of docosahexaenoic acid. J. Lipid Res. *42*, 1987–1995.

25. Schram, A.W., Goldfischer, S., van Roermund, C.W., Brouwer-Kelder, E.M., Collins, J., Hashimoto, T., Heymans, H.S., van den Bosch, H., Schutgens, R.B., and Tager, J.M. (1987). Human peroxisomal 3-oxoacyl-coenzyme A thiolase deficiency. Proc. Natl. Acad. Sci. U. S. A. *84*, 2494–2496. https://doi.org/10.1073/pnas.84.8.2494.

26. Nagan, N., and Zoeller, R.A. (2001). Plasmalogens: biosynthesis and functions. Prog. Lipid Res. *40*, 199–229. https://doi.org/10.1016/s0163-7827(01)00003-0.

27. De Biase, I., Tortorelli, S., Kratz, L., J. Steinberg, S., Cusmano-Ozog, K., and Braverman, N. (2020). Laboratory diagnosis of disorders of peroxisomal biogenesis and function: a technical standard of the American College of Medical Genetics and Genomics (ACMG). Genet. Med. *22*, 686–697. https://doi.org/10.1038/s41436-019-0713-9.

28. Verhoeven, N.M., Roe, D.S., Kok, R.M., Wanders, R.J.A., Jakobs, C., and Roe, C.R. (1998). Phytanic acid and pristanic acid are oxidized by sequential peroxisomal and mitochondrial reactions in cultured fibroblasts. J. Lipid Res. *39*, 66–74. https://doi.org/10.1016/s0022-2275(20)34204-8.

29. Wanders, R.J.A., Vreken, P., Ferdinandusse, S., Jansen, G.A., Waterham, H.R., Van Roermund, C.W.T., and Van Grunsven, E.G. (2001). Peroxisomal fatty acid α- and *β*-oxidation in humans: enzymology, peroxisomal metabolite transporters and peroxisomal diseases. Biochem. Soc. Trans. *29*, 250–267. https://doi.org/10.1042/bst0290250.

30. Xu, S., Zou, F., Diao, Z., Zhang, S., Deng, Y., Zhu, X., Cui, L., Yu, J., Zhang, Z., Bamigbade, A.T., et al. (2019). Perilipin 2 and lipid droplets provide reciprocal stabilization. Biophys. Rep. *5*, 145–160. https://doi.org/10.1007/s41048-019-0091-5.

31. Domenichiello, A.F., Kitson, A.P., and Bazinet, R.P. (2015). Is docosahexaenoic acid synthesis from α-linolenic acid sufficient to supply the adult brain? Prog. Lipid Res. *59*, 54–66. https://doi.org/10.1016/j.plipres.2015.04.002.

32. SanGiovanni, J.P., and Chew, E.Y. (2005). The role of omega-3 long-chain polyunsaturated fatty acids in health and disease of the retina. Prog. Retin. Eye Res. *24*, 87–138. https://doi.org/10.1016/j.preteyeres.2004.06.002.

33. Brossard, N., Croset, M., Pachiaudi, C., Riou, J.P., Tayot, J.L., and Lagarde, M. (1996). Retroconversion and metabolism of [13C]22:6n-3 in humans and rats after intake of a single dose of [13C]22:6n-3-triacylglycerols. Am. J. Clin. Nutr. *64*, 577–586. https://doi.org/10.1093/ajcn/64.4.577.

34. Guo, X.-F., Tong, W.-F., Ruan, Y., Sinclair, A.J., and Li, D. (2020). Different metabolism of EPA, DPA and DHA in humans: A double-blind cross-over study. Prostaglandins Leukot. Essent. Fatty Acids *158*, 102033. https://doi.org/10.1016/j.plefa.2019.102033.

35. Metherel, A.H., Lacombe, R.J.S., Chouinard-Watkins, R., and Bazinet, R.P. (2019). Docosahexaenoic acid is both a product of and a precursor to tetracosahexaenoic acid in the rat. J. Lipid Res. *60*, 412–420. https://doi.org/10.1194/jlr.M090373.

36. Pal, A., Metherel, A.H., Fiabane, L., Buddenbaum, N., Bazinet, R.P., and Shaikh, S.R. (2020). Do Eicosapentaenoic Acid and Docosahexaenoic Acid Have the Potential to Compete against Each Other? Nutrients *12*. https://doi.org/10.3390/nu12123718.

37. Mariamenatu, A.H., and Abdu, E.M. (2021). Overconsumption of Omega-6 Polyunsaturated Fatty Acids (PUFAs) versus Deficiency of Omega-3 PUFAs in Modern-Day Diets: The Disturbing Factor for Their "Balanced Antagonistic Metabolic Functions" in the Human Body. J. Lipids *2021*, 8848161. https://doi.org/10.1155/2021/8848161.

38. Di Cara, F., Sheshachalam, A., Braverman, N.E., Rachubinski, R.A., and Simmonds, A.J. (2017). Peroxisome-Mediated Metabolism Is Required for Immune Response to Microbial Infection. Immunity *47*, 93-106.e7. https://doi.org/10.1016/j.immuni.2017.06.016.

39. Nath, A.S., Parsons, B.D., Makdissi, S., Chilvers, R.L., Mu, Y., Weaver, C.M., Euodia, I., Fitze, K.A., Long, J., Scur, M., et al. (2022). Modulation of the cell membrane lipid milieu by peroxisomal β-oxidation induces Rho1 signaling to trigger inflammatory responses. Cell Rep. *38*, 110433. https://doi.org/10.1016/j.celrep.2022.110433.

40. Zhang, Q., Presswalla, F., Feathers, K., Cao, X., Hughes, B.A., Zacks, D.N., Thompson, D.A., and Miller, J.M.L. (2019). A platform for assessing outer segment fate in primary human fetal RPE cultures. Exp. Eye Res. *178*, 212–222. https://doi.org/10.1016/j.exer.2018.10.008.

41. Sergi, D., Zauli, E., Casciano, F., Secchiero, P., Zauli, G., Fields, M., and Melloni, E. (2022). Palmitic Acid Induced a Long-Lasting Lipotoxic Insult in Human Retinal Pigment Epithelial Cells, which Is Partially Counteracted by TRAIL. Antioxidants *11*, 2340. https://doi.org/10.3390/antiox11122340.

42. Benson, M.D., Papp, K.M., Casey, G.A., Radziwon, A., St Laurent, C.D., Doucette, L.P., and MacDonald, I.M. (2021). PEX6 Mutations in Peroxisomal Biogenesis Disorders. Ophthalmol. Sci. *1*, 100028. https://doi.org/10.1016/j.xops.2021.100028.

43. Daich Varela, M., Jani, P., Zein, W.M., D'Souza, P., Wolfe, L., Chisholm, J., Zalewski, C., Adams, D., Warner, B.M., Huryn, L.A., et al. (2020). The peroxisomal disorder spectrum and Heimler syndrome: Deep phenotyping and review of the literature. Am. J. Med. Genet. C Semin. Med. Genet. *184*, 618–630. https://doi.org/10.1002/ajmg.c.31823.

44. Bharti, K., Den Hollander, A.I., Lakkaraju, A., Sinha, D., Williams, D.S., Finnemann, S.C., Bowes-Rickman, C., Malek, G., and D'Amore, P.A. (2022). Cell culture models to study retinal pigment epithelium-related pathogenesis in age-related macular degeneration. Exp. Eye Res. *222*, 109170. https://doi.org/10.1016/j.exer.2022.109170.

45. Ferrington, D.A., Ebeling, M.C., Kapphahn, R.J., Terluk, M.R., Fisher, C.R., Polanco, J.R., Roehrich, H., Leary, M.M., Geng, Z., Dutton, J.R., et al. (2017). Altered bioenergetics and enhanced resistance to oxidative stress in human retinal pigment epithelial cells from donors with age-related macular degeneration. Redox Biol. *13*, 255–265. https://doi.org/10.1016/j.redox.2017.05.015.

46. Markert, E.K., Klein, H., Viollet, C., Rust, W., Strobel, B., Kauschke, S.G., Makovoz, B., Neubauer, H., Bakker, R.A., and Blenkinsop, T.A. (2022). Transcriptional comparison of adult human primary Retinal Pigment Epithelium, human pluripotent stem cell-derived Retinal Pigment Epithelium, and ARPE19 cells. Front. Cell Dev. Biol. *10*, 910040. https://doi.org/10.3389/fcell.2022.910040.

47. Wang, X.-M., Yik, W.Y., Zhang, P., Lu, W., Huang, N., Kim, B.R., Shibata, D., Zitting, M., Chow, R.H., Moser, A.B., et al. (2015). Induced pluripotent stem cell models of Zellweger spectrum disorder show impaired peroxisome assembly and cell type-specific lipid abnormalities. Stem Cell Res. Ther. *6*, 158. https://doi.org/10.1186/s13287-015-0149-3.

48. Pellegrino, E., Aylan, B., Bussi, C., Fearns, A., Bernard, E.M., Athanasiadi, N., Santucci, P., Botella, L., and Gutierrez, M.G. (2023). Peroxisomal ROS control cytosolic Mycobacterium tuberculosis replication in human macrophages. J. Cell Biol. *222*. https://doi.org/10.1083/jcb.202303066.

49. Judy, R.M., Sheedy, C.J., and Gardner, B.M. (2022). Insights into the Structure and Function of the Pex1/Pex6 AAA-ATPase in Peroxisome Homeostasis. Cells *11*, 2067. https://doi.org/10.3390/cells11132067.

50. Dodt, G., and Gould, S.J. (1996). Multiple PEX genes are required for proper subcellular distribution and stability of Pex5p, the PTS1 receptor: evidence that PTS1 protein import is mediated by a cycling receptor. J. Cell Biol. *135*, 1763–1774. https://doi.org/10.1083/jcb.135.6.1763.

51. Yahraus, T., Braverman, N., Dodt, G., Kalish, J.E., Morrell, J.C., Moser, H.W., Valle, D., and Gould, S.J. (1996). The peroxisome biogenesis disorder group 4 gene, PXAAA1, encodes a cytoplasmic ATPase required for stability of the PTS1 receptor. EMBO J. *15*, 2914–2923.

52. Wang, W., and Subramani, S. (2017). Role of PEX5 ubiquitination in maintaining peroxisome dynamics and homeostasis. Cell Cycle Georget. Tex *16*, 2037–2045. https://doi.org/10.1080/15384101.2017.1376149.

53. Sheedy, C.J., Chowdhury, S.P., Ali, B.A., Miyamoto, J., Pang, E.Z., Bacal, J., Tavasoli, K.U., Richardson, C.D., and Gardner, B.M. (2025). PEX1G843D remains functional in peroxisome biogenesis but is rapidly degraded by the proteasome. J. Biol. Chem. *301*, 108467. https://doi.org/10.1016/j.jbc.2025.108467.

54. Juszkiewicz, S., and Hegde, R.S. (2018). Quality Control of Orphaned Proteins. Mol. Cell *71*, 443–457. https://doi.org/10.1016/j.molcel.2018.07.001.

55. Law, K.B., Bronte-Tinkew, D., Di Pietro, E., Snowden, A., Jones, R.O., Moser, A., Brumell, J.H., Braverman, N., and Kim, P.K. (2017). The peroxisomal AAA ATPase complex prevents pexophagy and development of peroxisome biogenesis disorders. Autophagy *13*, 868–884. https://doi.org/10.1080/15548627.2017.1291470.

56. Smith, J.J., and Aitchison, J.D. (2013). Peroxisomes take shape. Nat. Rev. Mol. Cell Biol. *14*, 803–817. https://doi.org/10.1038/nrm3700.

57. Braverman, N.E., Raymond, G.V., Rizzo, W.B., Moser, A.B., Wilkinson, M.E., Stone, E.M., Steinberg, S.J., Wangler, M.F., Rush, E.T., Hacia, J.G., et al. (2016). Peroxisome biogenesis disorders in the Zellweger spectrum: An overview of current diagnosis, clinical manifestations, and treatment guidelines. Mol. Genet. Metab. *117*, 313–321. https://doi.org/10.1016/j.ymgme.2015.12.009.

58. Steinberg, S.J., Dodt, G., Raymond, G.V., Braverman, N.E., Moser, A.B., and Moser, H.W. (2006). Peroxisome biogenesis disorders. Biochim. Biophys. Acta *1763*, 1733–1748. https://doi.org/10.1016/j.bbamcr.2006.09.010.

59. Takemoto, Y., Suzuki, Y., Horibe, R., Shimozawa, N., Wanders, R.J.A., and Kondo, N. (2003). Gas chromatography/mass spectrometry analysis of very long chain fatty acids, docosahexaenoic acid, phytanic acid and plasmalogen for the screening of peroxisomal disorders. Brain Dev. *25*, 481–487. https://doi.org/10.1016/s0387-7604(03)00033-0.

60. Omri, S., Argyriou, C., Pryce, R.S., Di Pietro, E., Chaurand, P., and Braverman, N. (2025). Spatial characterization of RPE structure and lipids in the PEX1-p.Gly844Asp mouse model for Zellweger spectrum disorder. J. Lipid Res. *66*, 100771. https://doi.org/10.1016/j.jlr.2025.100771.

61. Mobley, J.A., Leav, I., Zielie, P., Wotkowitz, C., Evans, J., Lam, Y.-W., L'Esperance, B.S., Jiang, Z., and Ho, S.-M. (2003). Branched fatty acids in dairy and beef products markedly enhance alpha-methylacyl-CoA racemase expression in prostate cancer cells in vitro. Cancer Epidemiol. Biomark. Prev. Publ. Am. Assoc. Cancer Res. Cosponsored Am. Soc. Prev. Oncol. *12*, 775–783.

62. Rüether, K., Baldwin, E., Casteels, M., Feher, M.D., Horn, M., Kuranoff, S., Leroy, B.P., Wanders, R.J., and Wierzbicki, A.S. (2010). Adult Refsum disease: a form of tapetoretinal dystrophy accessible to therapy. Surv. Ophthalmol. *55*, 531–538. https://doi.org/10.1016/j.survophthal.2010.03.007.

63. Rönicke, S., Kruska, N., Kahlert, S., and Reiser, G. (2009). The influence of the branched-chain fatty acids pristanic acid and Refsum disease-associated phytanic acid on mitochondrial functions and calcium regulation of hippocampal neurons, astrocytes, and oligodendrocytes. Neurobiol. Dis. *36*, 401–410. https://doi.org/10.1016/j.nbd.2009.08.005.

64. Bernstein, P.S., Lloyd, M.B., O'Day, W.T., and Bok, D. (1992). Effect of phytanic acid on cultured retinal pigment epithelium: an in vitro model for Refsum's disease. Exp. Eye Res. *55*, 869–878. https://doi.org/10.1016/0014-4835(92)90013-i.

65. Kwon, W., and Freeman, S.A. (2020). Phagocytosis by the Retinal Pigment Epithelium: Recognition, Resolution, Recycling. Front. Immunol. *11*, 604205. https://doi.org/10.3389/fimmu.2020.604205.

66. Chang, C.-L., Weigel, A.V., Ioannou, M.S., Pasolli, H.A., Xu, C.S., Peale, D.R., Shtengel, G., Freeman, M., Hess, H.F., Blackstone, C., et al. (2019). Spastin tethers lipid droplets to peroxisomes and directs fatty acid trafficking through ESCRT-III. J. Cell Biol. *218*, 2583–2599. https://doi.org/10.1083/jcb.201902061.

67. Ding, L., Sun, W., Balaz, M., He, A., Klug, M., Wieland, S., Caiazzo, R., Raverdy, V., Pattou, F., Lefebvre, P., et al. (2021). Peroxisomal β-oxidation acts as a sensor for intracellular fatty acids and regulates lipolysis. Nat. Metab. *3*, 1648–1661. https://doi.org/10.1038/s42255-021-00489-2.

68. Chu, B.-B., Liao, Y.-C., Qi, W., Xie, C., Du, X., Wang, J., Yang, H., Miao, H.-H., Li, B.-L., and Song, B.-L. (2015). Cholesterol Transport through Lysosome-Peroxisome Membrane Contacts. Cell *161*, 291–306. https://doi.org/10.1016/j.cell.2015.02.019.

69. Srinivasan, B., Kolli, A.R., Esch, M.B., Abaci, H.E., Shuler, M.L., and Hickman, J.J. (2015). TEER Measurement Techniques for In Vitro Barrier Model Systems. SLAS Technol. *20*, 107–126. https://doi.org/10.1177/2211068214561025.

70. Fliesler, S.J., and Anderson, R.E. (1983). Chemistry and metabolism of lipids in the vertebrate retina. Prog. Lipid Res. *22*, 79–131. https://doi.org/10.1016/0163-7827(83)90004-8.

71. Swinkels, D., and Baes, M. (2023). The essential role of docosahexaenoic acid and its derivatives for retinal integrity. Pharmacol. Ther. *247*, 108440. https://doi.org/10.1016/j.pharmthera.2023.108440.

72. Sprecher, H., Luthria, D.L., Mohammed, B.S., and Baykousheva, S.P. (1995). Reevaluation of the pathways for the biosynthesis of polyunsaturated fatty acids. J. Lipid Res. *36*, 2471–2477.

73. Su, H.M., Moser, A.B., Moser, H.W., and Watkins, P.A. (2001). Peroxisomal straight-chain Acyl-CoA oxidase and D-bifunctional protein are essential for the retroconversion step in docosahexaenoic acid synthesis. J. Biol. Chem. *276*, 38115–38120. https://doi.org/10.1074/jbc.M106326200.

74. Voss, A., Reinhart, M., Sankarappa, S., and Sprecher, H. (1991). The metabolism of 7,10,13,16,19docosapentaenoic acid to 4,7,10,13,16,19-docosahexaenoic acid in rat liver is independent of a 4-desaturase. J. Biol. Chem. *266*, 19995–20000.

75. Grønn, M., Christensen, E., Hagve, T.A., and Christophersen, B.O. (1991). Peroxisomal retroconversion of docosahexaenoic acid (22:6(n-3)) to eicosapentaenoic acid (20:5(n-3)) studied in isolated rat liver cells. Biochim. Biophys. Acta *1081*, 85–91. https://doi.org/10.1016/00052760(91)90254-f.

76. Yu, M., Benham, A., Logan, S., Brush, R.S., Mandal, M.N.A., Anderson, R.E., and Agbaga, M.-P. (2012). ELOVL4 protein preferentially elongates 20:5n3 to very long chain PUFAs over 20:4n6 and 22:6n3. J. Lipid Res. *53*, 494–504. https://doi.org/10.1194/jlr.M021386.

77. Boeck, M., Yagi, H., Chen, C.T., Zeng, Y., Lee, D., Nian, S., Kasai, T., Lee, J., Hirst, V., Wang, C., et al. (2025). Nutrient supplementation mitigates retinal dysfunction in Acox1 knockout mice with impaired peroxisomal fatty acid oxidation. J. Adv. Res., S2090123225001456. https://doi.org/10.1016/j.jare.2025.03.004.

78. Anderson, R.E., and Maude, M.B. (1970). Lipids of ocular tissues. 6. Phospholipids of bovine rod outer segments. Biochemistry *9*, 3624–3628. https://doi.org/10.1021/bi00820a019.

79. Avery, S., Hirst, A.J., Baker, D., Lim, C.Y., Alagaratnam, S., Skotheim, R.I., Lothe, R.A., Pera, M.F., Colman, A., Robson, P., et al. (2013). BCL-XL mediates the strong selective advantage of a 20q11.21 amplification commonly found in human embryonic stem cell cultures. Stem Cell Rep. *1*, 379–386. https://doi.org/10.1016/j.stemcr.2013.10.005.

Figures

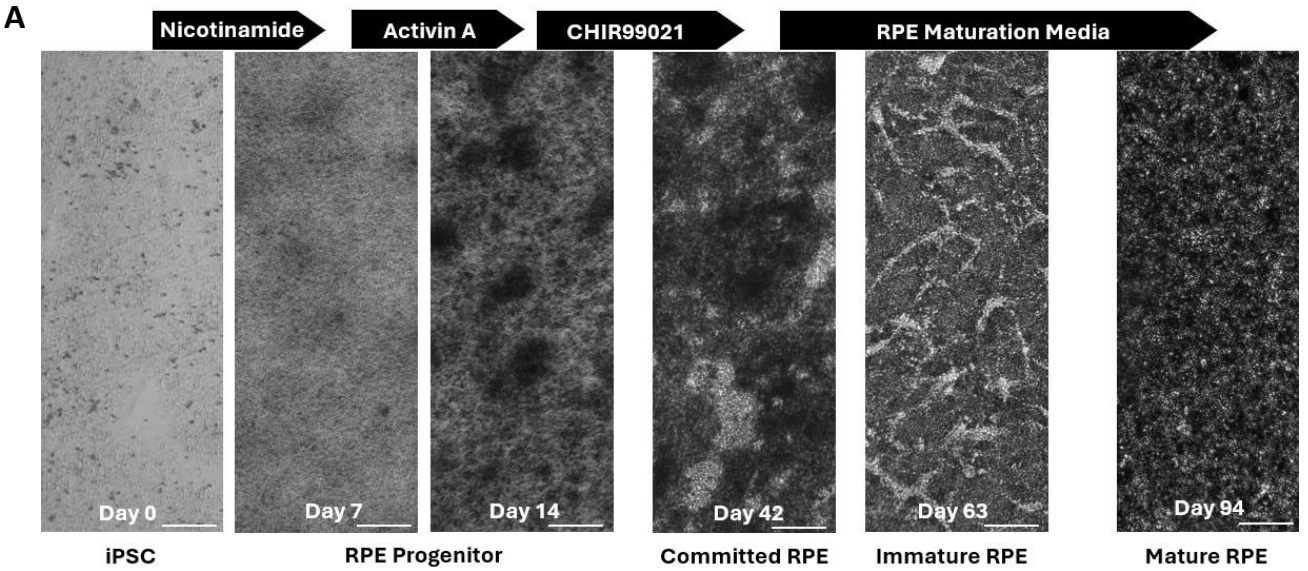

B

iRPE-Signature Protein	Wildtype	*PEX1*$^{-/-}$	*PEX6*$^{-/-}$
TYRP1	88.6%	93.5%	82.6%
PAX6	90.7%	94.7%	85.9%
PMEL17	92.1%	93.8%	92.4%
BEST1	91.5%	93.5%	91.6%
MITF	90.4%	92.8%	90.5%

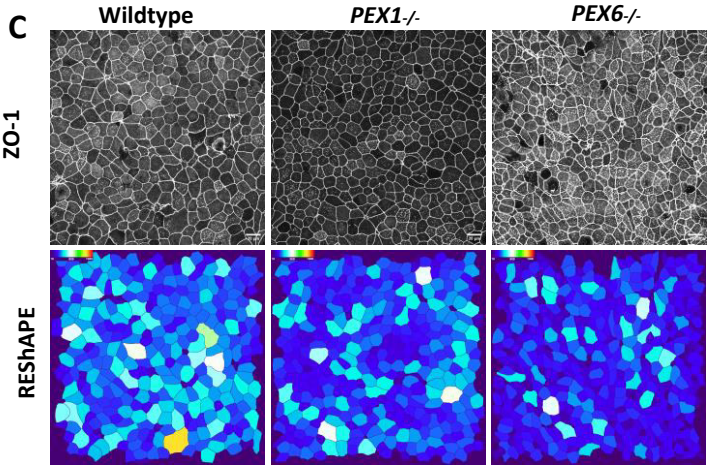

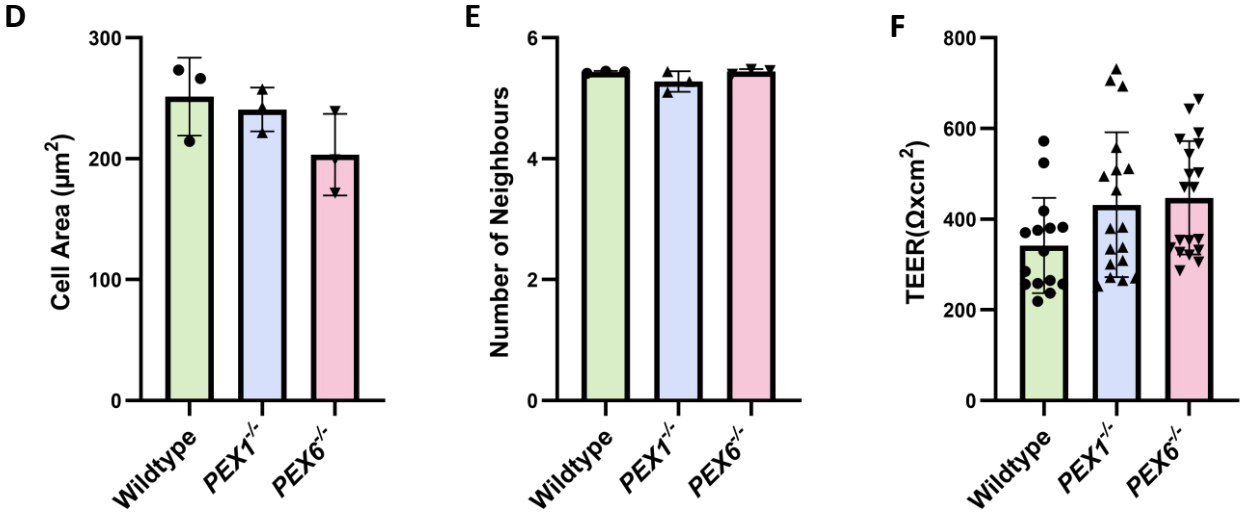

Figure 1: Differentiation and characterization of iPSC-RPE (iRPE) with PEX mutations.

(A) Representative brightfield images highlighting the differentiation timeline and media supplements. Scale bar = 350 µm.
(B) RPE signature proteins detected from iRPE populations assayed using flow cytometry. At least 10,000 events were captured for each sample.
(C) Representative confocal microscopy images of iRPE showing maximum intensity projections of anti-Zonula Occludens-1 (ZO-1), a tight junction protein, and corresponding REShAPE cell area heat maps. Scale bar = 20 µm.
(D) Mean iRPE area and standard deviation following REShAPE analysis. One-way ANOVA p=0.18 (n=3).
(E) Mean number of neighboring iRPE cells and standard deviation following REShAPE analysis. One-way ANOVA p=0.16 (n=3).
(F) Transepithelial electrical resistance (TEER) of iRPE cultured on 0.33 cm^2 transwells. One-way ANOVA p=0.063 (n=15).

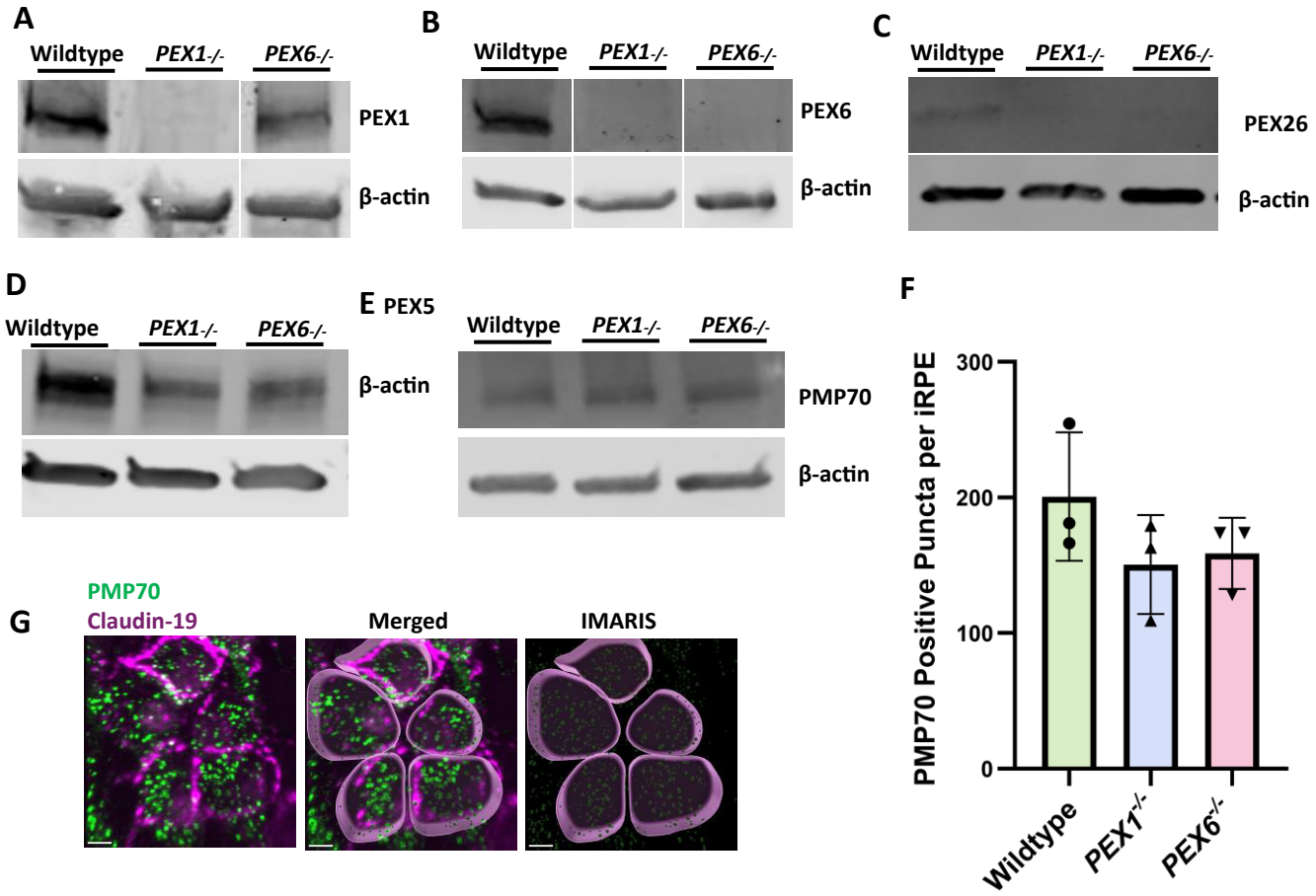

Figure 2: Consequences of knockout of PEX1 and PEX6 on peroxisome abundance and associated PEX proteins in iRPE.

(A) Representative immunoblot of iRPE lysates using anti-PEX1 and anti-β-actin antibodies. 50 µ g of protein was loaded per lane (n=3).
(B) Representative immunoblot of iRPE lysates using anti-PEX6 and anti-β-actin antibodies. 50 µ g of protein was loaded per lane (n=3).
(C) Representative immunoblot of iRPE lysates using anti-PEX26 and anti-β-actin antibodies. 30 µg of protein was loaded per lane (n=3).
(D) Representative immunoblot of iRPE lysates using anti-PEX5 and anti-β-actin antibodies. 30 µ g of protein was loaded per lane (n=3).
(E) Representative immunoblot of iRPE lysates using anti-PMP70 and anti-β-actin antibodies. 30 µg of protein was loaded per lane (n=3).
(F) Mean (± standard deviation) number of PMP70 spots detected per iRPE. 385 cells were analyzed in total (n=3).
(G) Representative confocal microscopy images of iRPE showing IMARIS rendering used for the quantification of PMP70 positive puncta, a marker for peroxisomes. Scale bar = 5 µm.

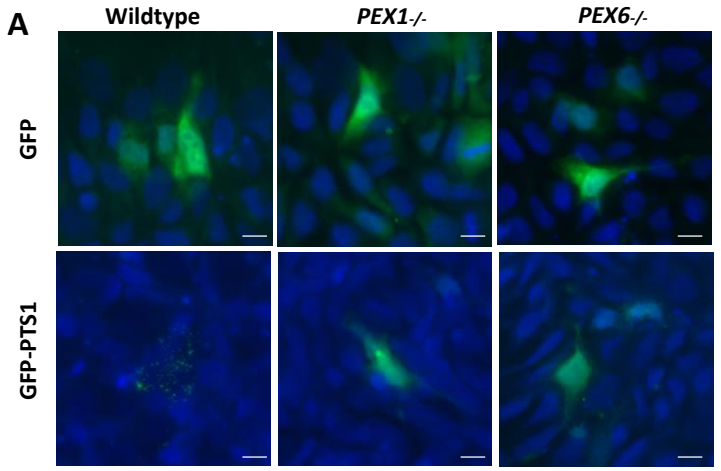
A
Wildtype
PEX1-/-
PEX6-/-
GFP
GFP-PTS1

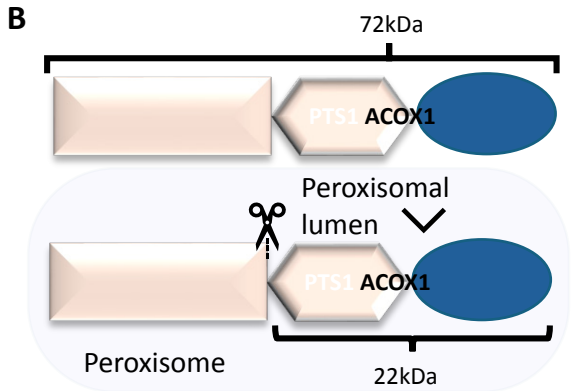
B
72kDa
PTS1
ACOX1
Peroxisomal lumen
PTS1
ACOX1
Peroxisome
22kDa

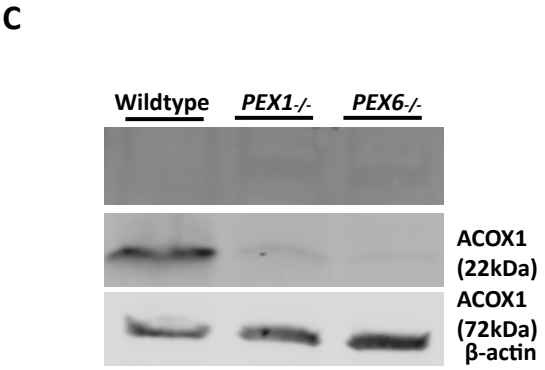
C
Wildtype
PEX1-/-
PEX6-/-
ACOX1 (22kDa)
ACOX1 (72kDa)
β-actin

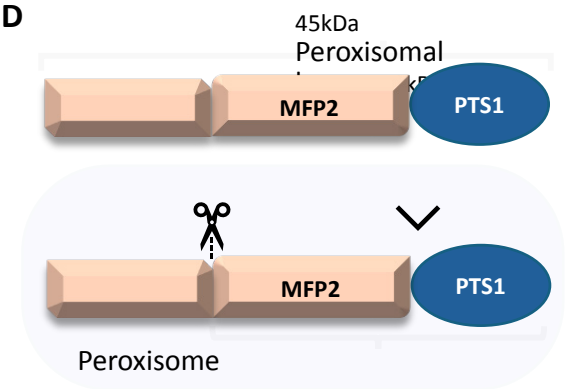
D
45kDa
Peroxisomal
MFP2
PTS1
MFP2
PTS1
Peroxisome

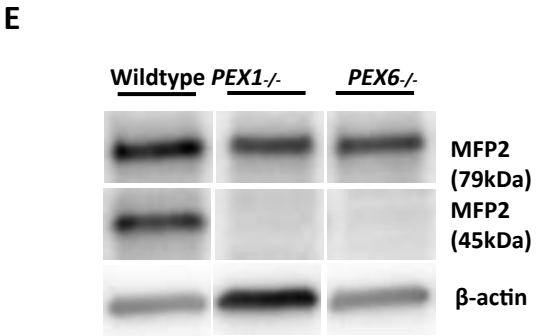
E
Wildtype
PEX1-/-
PEX6-/-
MFP2 (79kDa)
MFP2 (45kDa)
β-actin

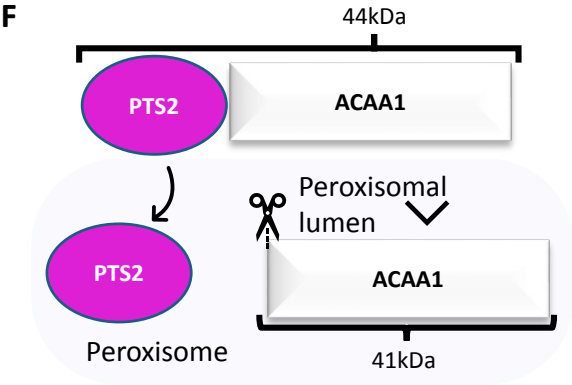
F
44kDa
PTS2
ACAA1
Peroxisomal lumen
PTS2
ACAA1
Peroxisome
41kDa

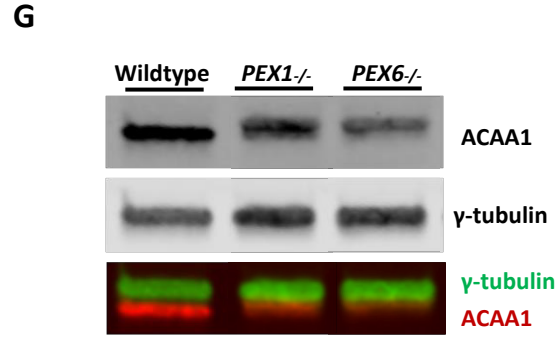
G
Wildtype
PEX1-/-
PEX6-/-
ACAA1
γ-tubulin
γ-tubulin
ACAA1

Figure 3: Knockout of PEX1 and PEX6 in iRPE results in peroxisomes with defective protein import.

(A) Representative widefield microscopy images of iPSCs transfected with GFP only or GFPPTS1 expression plasmids. PTS1 targets proteins to the peroxisome matrix. Scale bar = 5μm.
(B) Schematic demonstrating the import of ACOX1 into peroxisomes, followed by its subsequent cleavage.
(C) Representative immunoblot of iRPE lysates using anti-ACOX1 and anti-β-actin antibodies. 50 μg of protein was loaded per lane (n=3).
(D) Schematic demonstrating the import of MFP2 into peroxisomes, followed by its subsequent cleavage.
(E) Representative immunoblot of iRPE lysates using anti-MFP2 and anti-β-actin antibodies. 10 μg of protein was loaded per lane (n=3).
(F) Schematic demonstrating the import of ACAA1 into peroxisomes, followed by its subsequent processing.
(G) Representative immunoblot of iRPE lysates using anti-ACAA1 and anti-γ-tubulin antibodies. 30 μg of protein was loaded per lane (n=3).

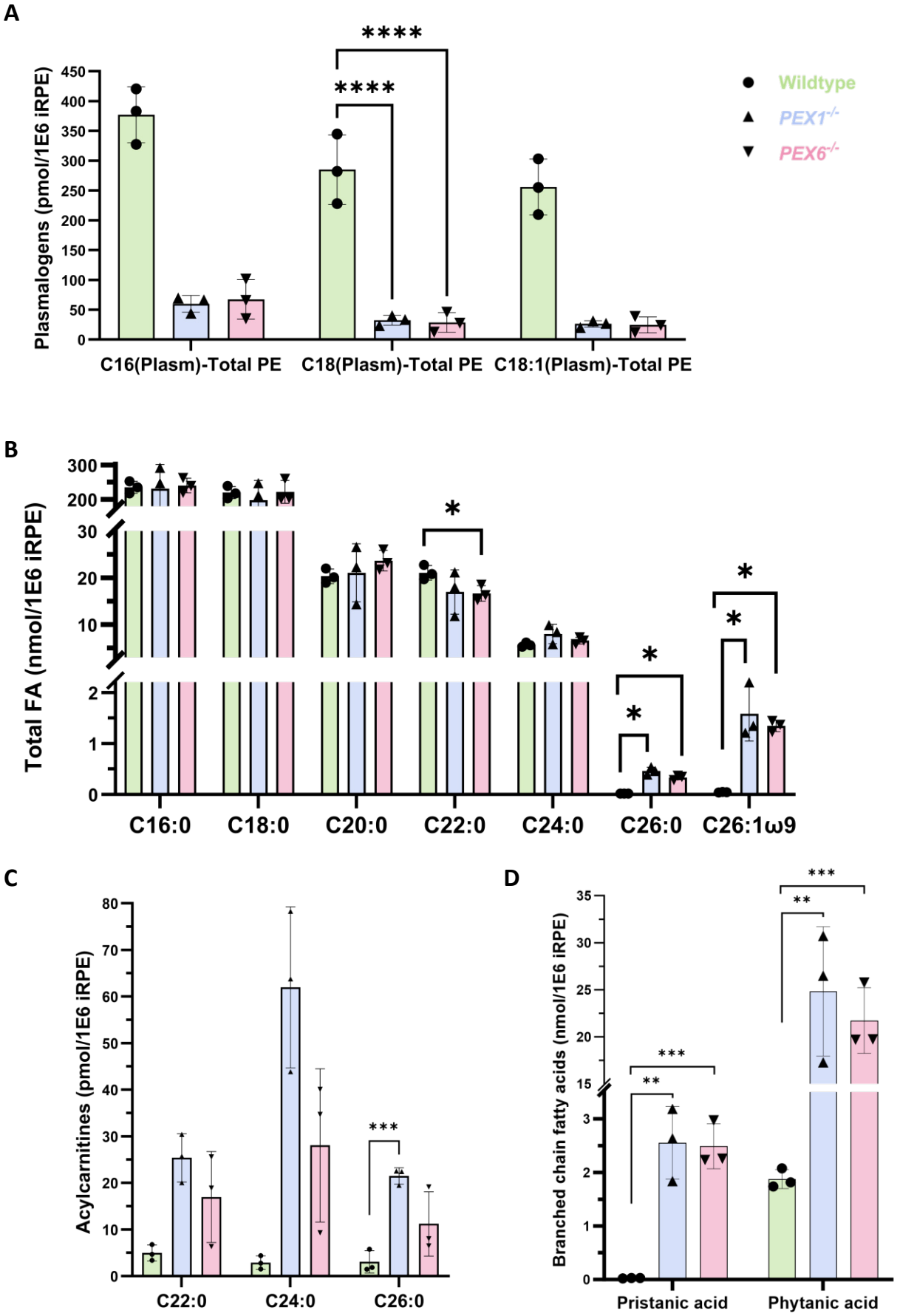
A
Plasmalogens (pmol/1E6 iRPE)
450
400
350
300
250
200
150
100
50
0
****
****
C16(Plasm)-Total PE
C18(Plasm)-Total PE
C18:1(Plasm)-Total PE
Wildtype
PEX1-/-
PEX6-/-
B
Total FA (nmol/1E6 iRPE)
300
200
30
20
10
2
1
0
*
*
*
*
*
C16:0
C18:0
C20:0
C22:0
C24:0
C26:0
C26:1ω9
C
Acylcarnitines (pmol/1E6 iRPE)
80
70
60
50
40
30
20
10
0
***
C22:0
C24:0
C26:0
D
Branched chain fatty acids (nmol/1E6 iRPE)
35
30
25
20
15
3
2
1
0
***
**
***
**
Pristanic acid
Phytanic acid

Figure 4: Quantitative analysis of fatty acids in PEX1 and PEX6 knockout iRPE at baseline.

(A) Quantification and comparison of plasmalogens in iRPE lysates measured by LC-MS. Multiple unpaired t tests were performed (n=3). Statistical analysis was only performed only on C18(Plasm)-Total PE because the other species were semi-quantitative.

(B) Quantification and comparison of very long-chain fatty acids (VLCFA) in iRPE lysates measured by GC-MS. Multiple unpaired t tests were performed (n=3).

(C) Quantification and comparison of acylcarnitines in iRPE lysates measured by LC-MS. An unpaired t test was performed on C26:0 only (as this was the only species with a standard available); p=0.00042 (n=3).

(D) Quantification and comparison of branched chain fatty acids in iRPE lysates measured by GC-MS. Multiple unpaired t tests were performed (n=3). *p<0.05; **p<0.01; ***p<0.001; ****p<0.0001

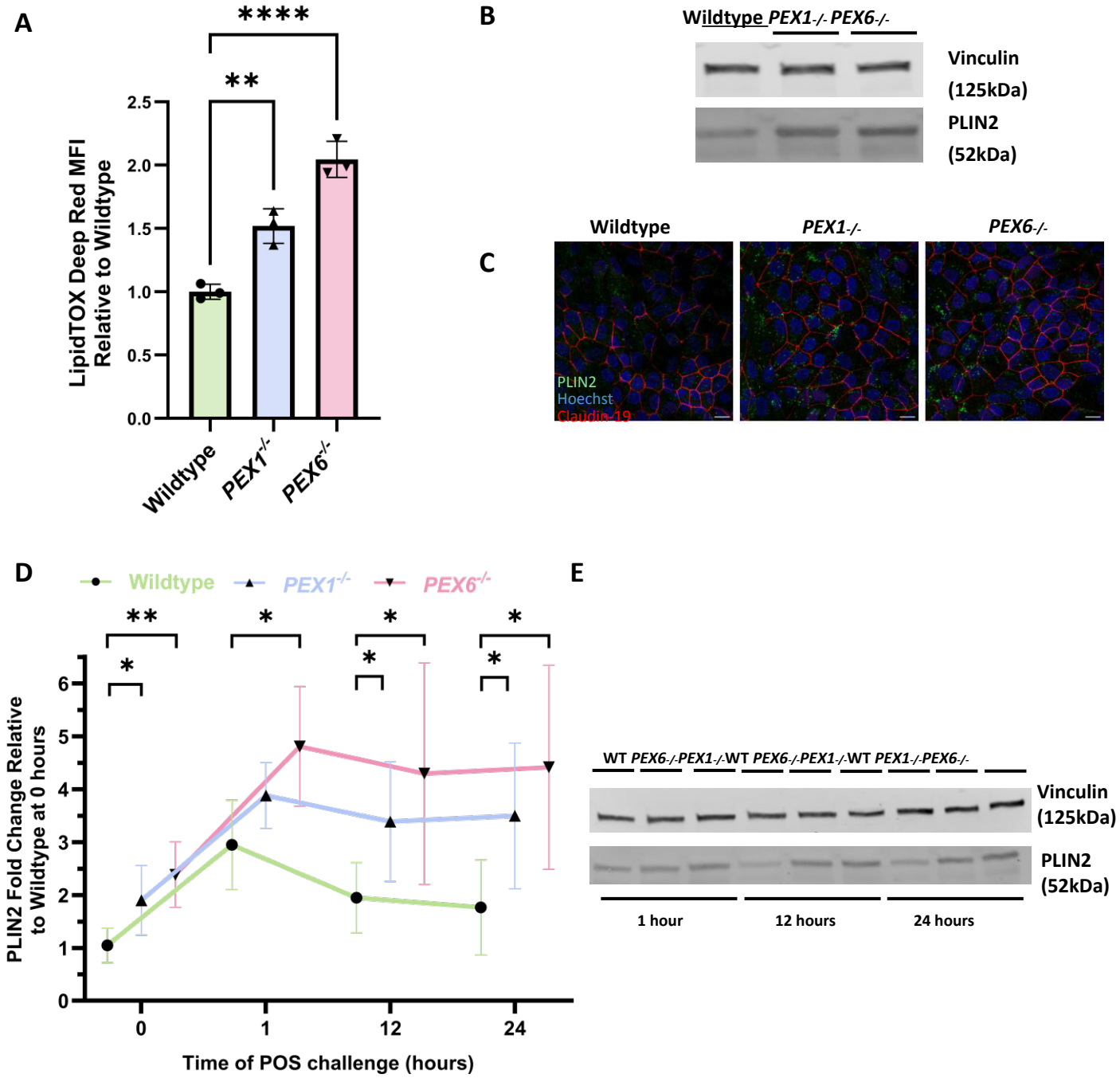

Figure 5: Lipid droplet perturbations in PEX1 and PEX6 knockout iRPE

(A) Median fluorescence intensity (MFI) of LipidTOX Deep Red, a neutral lipid dye, in iRPE captured by flow cytometry. At least 100,000 events were captured for each sample. One-way ANOVA p=0.014 (n=3). A Holm-Šídák multiple comparisons test was performed.

(B) Representative immunoblot of baseline lipid droplets in iRPE lysates using anti-PLIN2, a lipid droplet protein. 30 µg of protein was loaded per lane (n=6).

(C) Representative confocal microscopy images of iRPE showing maximum intensity projections of Hoechst, PLIN2, and Claudin-19 at baseline. Scale bar = 10 µm.

(D) Immunoblot quantification of PLIN2 densitometry (normalized to vinculin) in iRPE lysates following a continuous POS challenge (0.5 POS per cell). Two-way ANOVA $p=6.2\text{x}10^{-7}$ for genotype variation, $p=6.7\text{x}10^{-6}$ for time variation (n=6). Multiple unpaired t tests were performed.

(E) Representative immunoblot of lipid droplets (anti-PLIN2) from iRPE lysates following a continuous POS challenge (0.5 POS per cell). 30 µg of protein was loaded per lane (n=6). *$p<0.05$; **$p<0.01$; ****$p<0.0001$

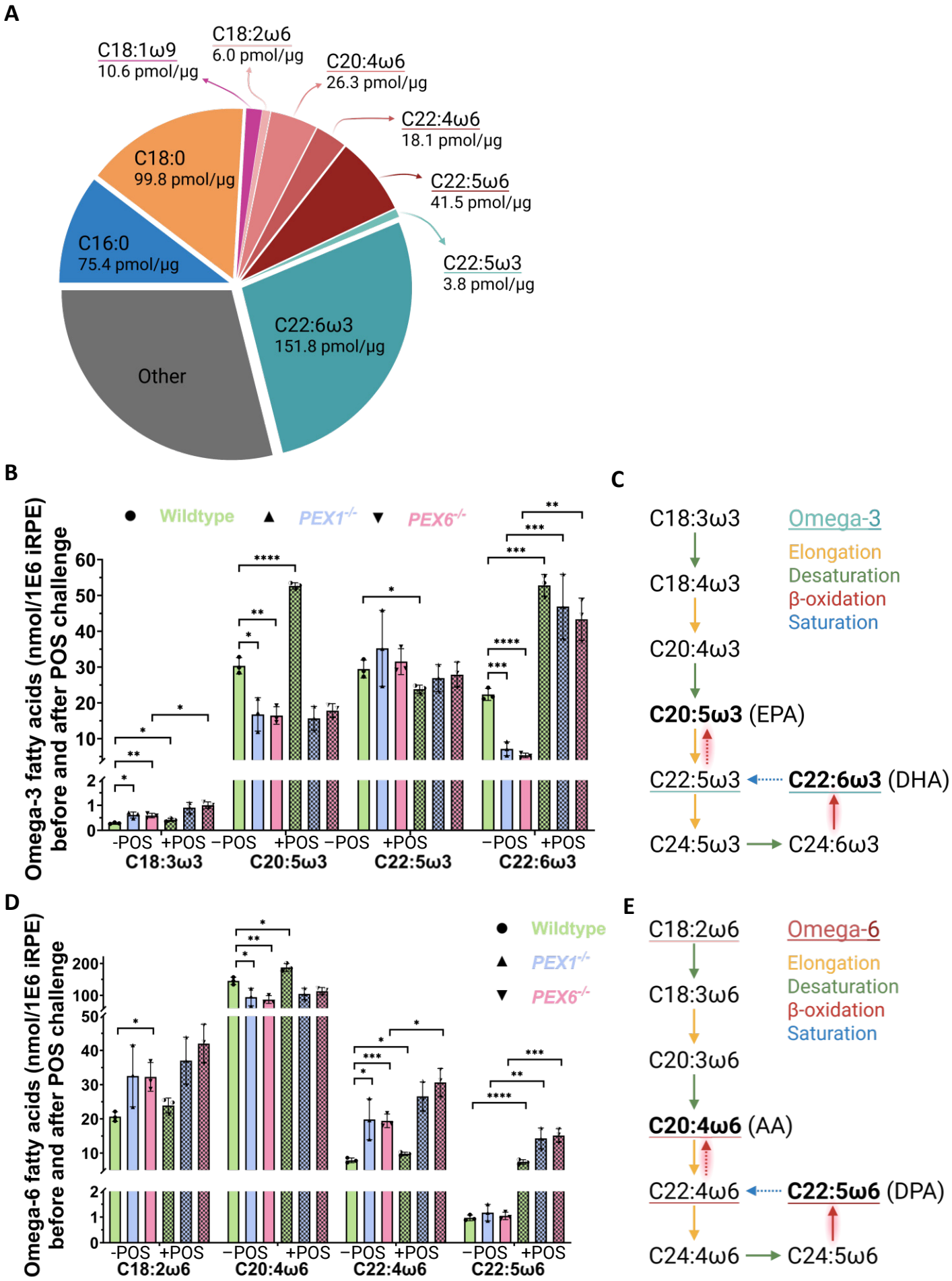
A
C18:1ω9
10.6 pmol/µg
C18:2ω6
6.0 pmol/µg
C20:4ω6
26.3 pmol/µg
C22:4ω6
18.1 pmol/µg
C22:5ω6
41.5 pmol/µg
C22:5ω3
3.8 pmol/µg
C22:6ω3
151.8 pmol/µg
Other
C16:0
75.4 pmol/µg
C18:0
99.8 pmol/µg
B
Wildtype
PEX1-/-
PEX6-/-
Omega-3 fatty acids (nmol/1E6 iRPE) before and after POS challenge
-POS +POS −POS +POS −POS +POS −POS +POS
C18:3ω3
C20:5ω3
C22:5ω3
C22:6ω3
C
C18:3ω3
C18:4ω3
C20:4ω3
C20:5ω3 (EPA)
C22:5ω3
C22:6ω3 (DHA)
C24:5ω3
C24:6ω3
Omega-3
Elongation
Desaturation
β-oxidation
Saturation
D
Wildtype
PEX1-/-
PEX6-/-
Omega-6 fatty acids (nmol/1E6 iRPE) before and after POS challenge
-POS +POS −POS +POS −POS +POS −POS +POS
C18:2ω6
C20:4ω6
C22:4ω6
C22:5ω6
E
C18:2ω6
C18:3ω6
C20:3ω6
C20:4ω6 (AA)
C22:4ω6
C22:5ω6 (DPA)
C24:4ω6
C24:5ω6
Omega-6
Elongation
Desaturation
β-oxidation
Saturation

Figure 6: Quantitative analysis of fatty acid profile changes in iRPE following a POS challenge.

(A) The most abundant fatty acid species detected by GC-MS from isolated bovine POS (n=3). Refer to Supplementary Table 2 for a complete list of detected fatty acid species.

(B) Quantification of omega-3 (ω3) fatty acids in iRPE lysates by GC-MS before and after a 7-day POS challenge (3 POS per cell were added with daily media changes). Two-way ANOVA $p=1.0\times10^{-15}$ for genotype variation, $p=6.1\times10^{-29}$ for fatty acid variation, and $p=2.1\times10^{-20}$ for the interaction (n=3). Multiple unpaired t tests were performed.

(C) The omega-3 fatty acid metabolic pathway adapted from Yu et al., 2012.[76] Reactions that are presumed to require intact peroxisome β-oxidation are highlighted in red.

(D) Quantification of omega-6 (ω6) fatty acids in iRPE lysates by GC-MS before and after a 7-day POS challenge (3 POS per cell were added with daily media changes). Two-way ANOVA $p=7.6\times10^{-7}$ for genotype variation, $p=1.9\times10^{-38}$ for fatty acid variation, and $p=2.6\times10^{-14}$ for the interaction (n=3). Multiple unpaired t tests were performed.

(E) The omega-6 fatty acid metabolic pathway adapted from Yu et al., 2012. [76] Reactions that are presumed to require intact peroxisome β-oxidation are highlighted in red.

*$p<0.05$; **$p<0.01$; ***$p<0.001$; ****$p<0.0001$

A

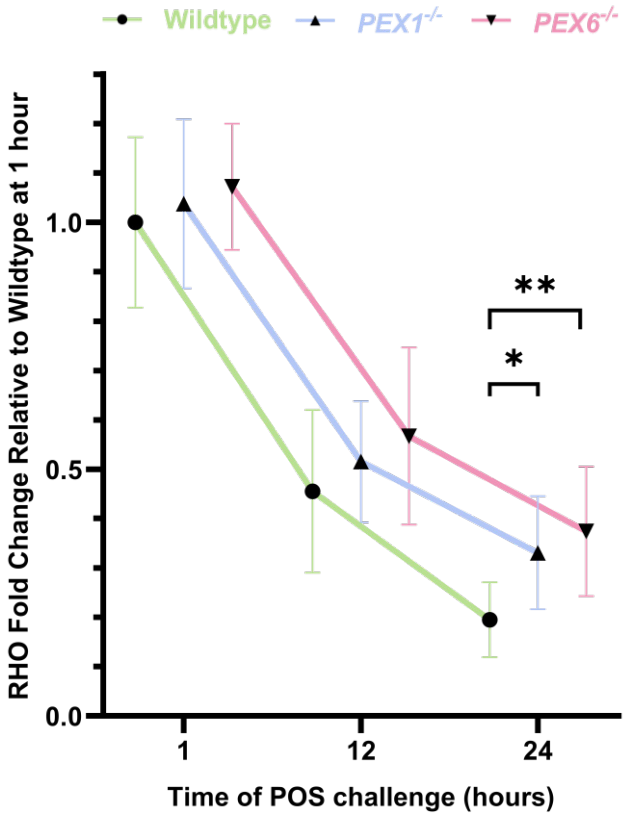
Wildtype
PEX1-/-
PEX6-/-
RHO Fold Change Relative to Wildtype at 1 hour
1.0
0.5
0.0
**
*
1
12
24
Time of POS challenge (hours)

B

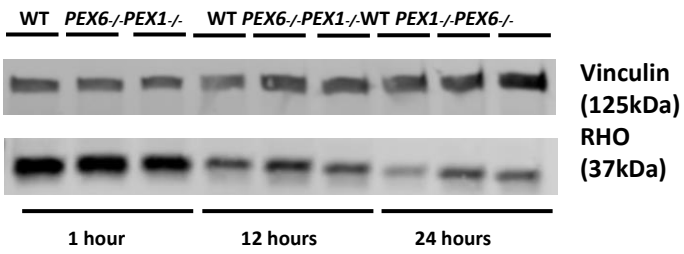
WT
PEX6-/-PEX1-/-
WT
PEX6-/-PEX1-/-
WT
PEX1-/-PEX6-/-
Vinculin (125kDa)
RHO (37kDa)
1 hour
12 hours
24 hours

C

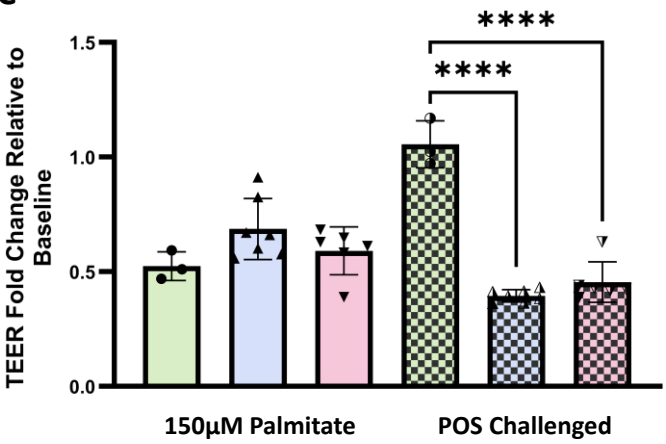
TEER Fold Change Relative to Baseline
1.5
1.0
0.5
0.0
****
****
150µM Palmitate
POS Challenged

D

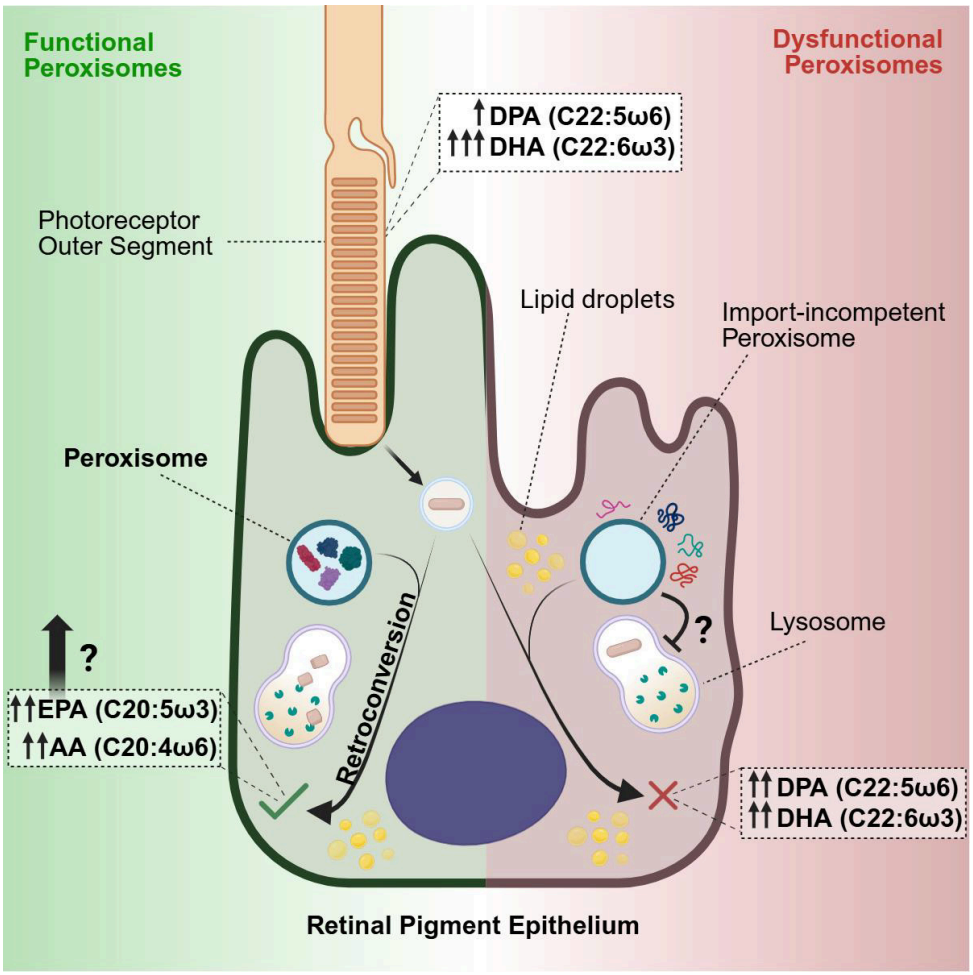
Functional Peroxisomes
Dysfunctional Peroxisomes
DPA (C22:5ω6)
DHA (C22:6ω3)
Photoreceptor Outer Segment
Lipid droplets
Import-incompetent Peroxisome
Peroxisome
Lysosome
?
?
EPA (C20:5ω3)
AA (C20:4ω6)
Retroconversion
DPA (C22:5ω6)
DHA (C22:6ω3)
Retinal Pigment Epithelium

Figure 7: Interrogating POS phagocytosis in PEX1 and PEX6 knockout iRPE.

(A) Quantification of changes in RHO densitometry by immunoblot in iRPE lysates following a continuous POS challenge (0.5 POS per cell). Two-way ANOVA p=0.021 for genotype and p=1.2x10^{-24} for time variations (n=8). Multiple unpaired t tests were performed.

(B) Representative immunoblots of iRPE lysates probed with anti-rhodopsin (RHO) and anti-vinculin antibodies (loading control) following a continuous POS challenge (0.5 POS per cell) (n=5).

(C) Relative fold change (compared to baseline) in transepithelial electrical resistance (TEER) of iRPE cultured on 0.33cm^2 transwells following a 24-hour incubation with 150 µM palmitate or POS (10 POS per cell). One-way ANOVA (POS challenge) p=1.2x10^{-8} (n=3). A Holm-Šídák multiple comparisons test was performed.

(D) Schematic summarizing the consequences of PEX1 and PEX6 knockout on iRPE biology, including the presence of import-incompetent peroxisomes, impaired ω3 and ω6 fatty acid retroconversion, lipid droplet accumulation, and defective POS phagocytosis.

*p<0.05; **p<0.01; ****p<0.0001

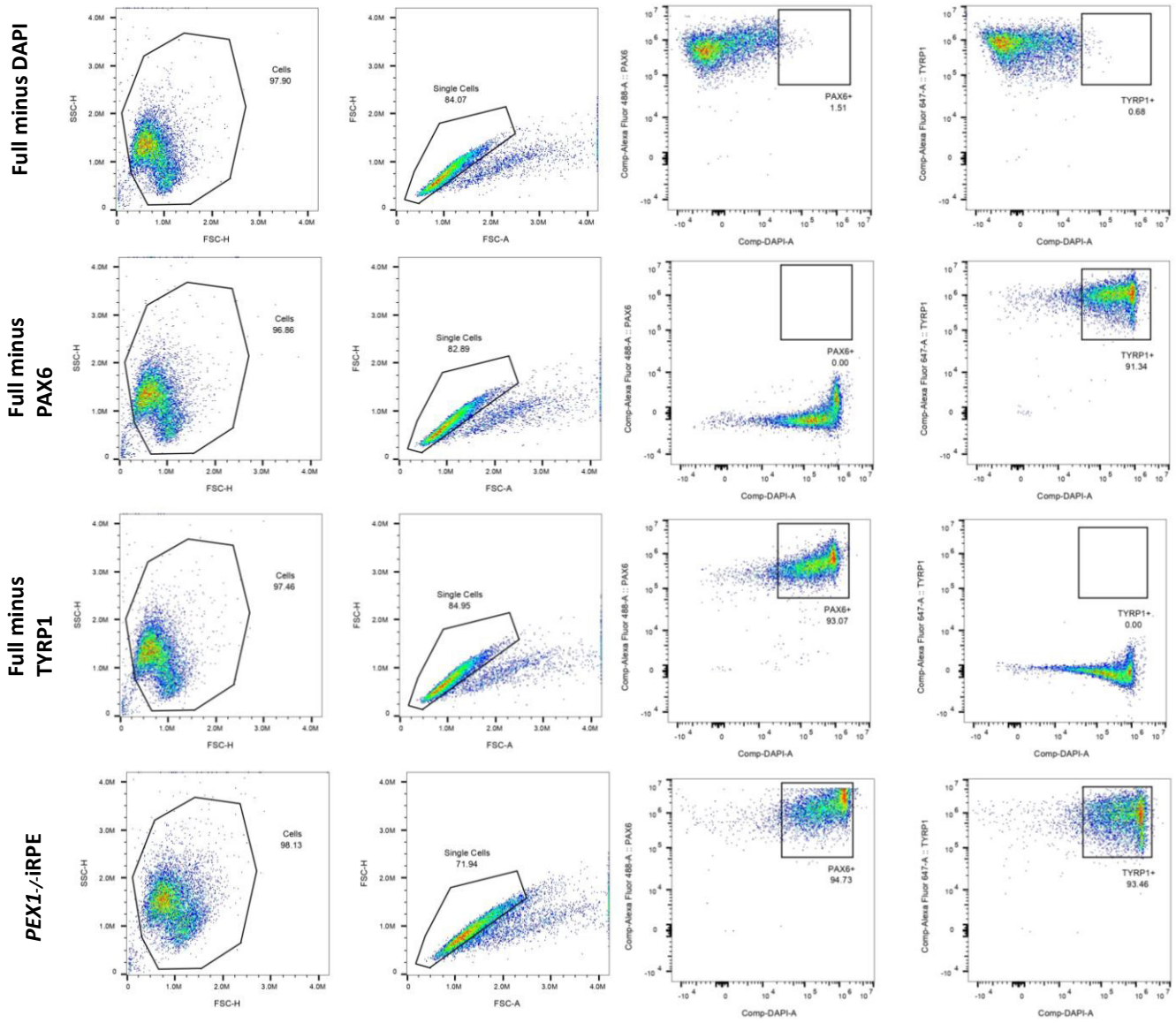

Supplementary Figure 5: Representative flow cytometry data showing gating strategies.